Electron heating and phase space signatures at supercritical, fast mode shocks

A. J. Hull,[1] J. D. Scudder,[2] D. E. Larson,[1] and R. Lin[1]

Abstract. We investigate the effect of the nonmonotonic features of the macroscopic magnetic field $B(x)$ and the deHoffmann-Teller frame electrostatic potential $\Phi^{HT}(x)$ on the electron distribution functions within collisionless, fast mode shocks. The signatures of electron distribution functions are explored by using Liouville's theorem in the adiabatic approximation to map model upstream and downstream boundary electron velocity distribution functions to regions inside model shocks with monotonic and nonmonotonic magnetic fields under the empirically motivated approximation that $\delta\Phi^{HT} \propto \delta B$. In the case of shocks with monotonically increasing magnetic fields, we show that there are no "exclusion" regions and that the electron distribution function at all pitch angles and hence the electron temperature increase can be explained by the reversible behavior of magnetized electrons in the shock macroscopic electric and magnetic fields. However, at shocks with nonmonotonic magnetic fields, there exist regions of inaccessibility which are outside the domain of the one-Dimensional (1-D), steady state Vlasov-Liouville (V-L) approach as defined by the upstream and downstream boundaries. Such regions, if occupied, may be filled by electrons scattered into these regions by waves, or perhaps by reversible processes such as the adiabatic convection of electrons into these regions of a curved bow shock, or by coherent nonadiabatic access. As a further test, the V-L method is employed to study, for the first time, the detailed signatures of full 3-D electron velocity distribution functions observed by the Wind spacecraft through the resolved layer of a supercritical, fast mode Earth bow shock crossing. We demonstrate that much of the complex structure of the observed electron distribution function within the shock layer can be explained by the motion of adiabatic electrons in the nonmonotonic shock macroscopic magnetic and electric fields. However, a significant portion of electron phase space appears to be the remnants of electron phase space holes. The mechanisms responsible for allowing electrons to gain access to the exclusion regions are not well understood and may have important implications on the thermodynamic properties of collisionless shocks.

1. Introduction

Early measurements of the electrons by the VELA and ISEE satellites in the vicinity of the Earth's bow shock have shown that the electron distribution function has a considerable amount of structure [e.g., *Montgomery et al.*, 1970; *Feldman et al.*, 1982, 1983; *Scudder et al.*, 1986a]. Electron velocity distribution functions on the preshocked (upstream) side near the shock magnetic ramp typically have an enhanced tail of high-energy electrons traveling away from the shock. With increasing penetration within the shock magnetic ramp into the postshocked (downstream) side of the shock, the electron distribution becomes increasingly flat-topped with a power law tail. A downstream directed, field-aligned beam is often found at the outer edge of the flat-top within the ramp that increases in mean energy and decreases in amplitude as one traverses the shock ramp from the upstream edge toward the downstream side of the shock. The electron beam subsequently merges into the nearly flat-topped part of the downstream distribution. The extreme deformation of the electron distribution occurs in the very thin region of the shock magnetic ramp giving rise to rather prompt changes in electron temperature which are roughly 2-4 times smaller than the ion temperature change ΔT_i [*Feldman*, 1985; *Schwartz et al.*, 1988].

Motivated by the apparent acceleration of the electron beams, *Feldman et al.* [1982] proposed a two-step

---

[1] Space Science Laboratory, University of California, Berkeley, Berkeley, California.

[2] Department of Physics and Astronomy, University of Iowa, Iowa City, Iowa.

process initiated by an acceleration by a field-aligned electric field followed by some beam-driven instability to explain the electron heating at the Earth's bow shock. *Balikhin et al.* [1993] and *Balikhin and Gedalin* [1994] invoked diverging electron trajectories as a mechanism responsible for the energization and heating of electrons, though this mechanism requires the shock to be sufficiently thin ($\sim c/\omega_{\rm pe}$) so that the guiding center ordered premise is no longer valid, a condition that may be realizable near 90° [*Tidman and Krall*, 1971]. Other studies [*Goodrich and Scudder*, 1984; *Scudder et al.*, 1986c; *Scudder*, 1995; *Hull et al.*, 1998; *Hull*, 1998] suggest that electron energization and hence the fluid electron temperature increase at both strong and weak collisionless shocks can be explained by the reversible guiding center ordered behavior of magnetized electrons in the smooth shock electric and magnetic forces. *Scudder et al.* [1986c] used $v_{\parallel} = 0$ cuts of electron distribution function measured at the upstream and downstream boundaries of the shock to infer the reversible expectation to regions within the resolved layer of a supercritical, fast mode shock using a Vlasov-Liouville (V-L) mapping approach. *Scudder et al.* [1986c] demonstrated that the effect of the shock electrostatic potential on deforming the field-aligned electron distribution function is significant and could possibly explain the electron heating morphology at these shocks. More recent complementary studies [*Scudder*, 1995; *Hull et al.*, 1998] demonstrated using model upstream electron distribution functions that the combined effects of the cross-shock macroscopic electric potential and magnetic field jump significantly broaden the electron distribution function at all pitch angles, providing support for the notion that the dc fields acting on magnetized electrons are responsible for the electron temperature changes at both strong and weak collisionless shocks. The preferential perpendicular enhancements to the electron distribution function typically observed to occur across weak shocks and the nearly isotropic enhancements to the electron distribution function observed across strong shocks are qualitatively recovered by the Vlasov model [*Scudder*, 1995; *Hull et al.*, 1998] without invoking wave particle effects.

Central to the V-L mapping approach is the determination of electron accessibility to regions within the shock and at the shock boundaries, which is very sensitive to the electrostatic potential and its functional relation to the magnetic field profile. Observations [*Hull et al.*, 2000] suggest that depending on β_e, the potential profile in the deHoffmann-Teller frame of reference (HTF) is approximately linearly related to the magnetic field profile, implying a functional relationship of the form $\delta\Phi^{\rm HT} = \kappa\delta{\rm B}$, where κ is a fixed constant for a given shock crossing. The HTF is defined as that special frame of reference in which the motional electric field vanishes in either side of the shock. In addition, *Scudder* [1987] demonstrated that the electron bulk velocity is approximately field aligned inside the shock layer,

provided electron inertia, electron anisotropy, and resistivity can be neglected as higher-order corrections. Consequently, electron energetics and electron temperature change is much simpler in HTF, with the typical electron being energized only by the parallel electric field as they traverse the shock [*Goodrich and Scudder*, 1984]. Although weak (subcritical) shocks tend to be characterized by monotonically increasing magnetic field profiles, strong (supercritical) shocks tend to have an overshoot-undershoot structure. In the theoretical studies by *Scudder* [1995] and *Hull et al.* [1998] the internal structure of the shock was ignored for simplicity to illustrate the effects of the cross-shock potential and magnetic field jump on the electron distribution function.

In this paper we explore the impact of both monotonic and nonmonotonic electric and magnetic field profiles on electron phase space topology and hence the impact on the electron distribution function within the resolved layer of collisionless, fast mode shocks. The purpose of this study is to clarify what aspects of the electron distribution and hence the temperature increase can and cannot be explained by the adiabatic motion of electrons in the shock macroscopic electromagnetic fields. This paper is an extension of previous studies on the signatures of electron distribution functions across supercritical shocks [e.g., *Feldman et al.*, 1983; *Scudder et al.*, 1986c; *Hull et al.*, 1997; *Hull*, 1998; *Gedalin and Griv*, 1999]. We provide a general framework based on Liouville's theorem for understanding electron phase space signatures at shocks with arbitrary magnetic field topologies under the empirically motivated hypothesis $\delta\Phi^{\rm HT} = \kappa\delta B$ [*Hull*, 1998; *Hull et al.*, 2000] in section 2. Our approach is similar to the V-L mapping approach employed by *Scudder et al.* [1986c], where the shock layer is described as a two-point boundary value problem. However, we study the effects of the shock macroscopic electromagnetic forces on the full three-Dimensional (3-D) electron distribution function within the shock layer proper. In this way we gain a more complete understanding of the properties the electron distribution function in response to the internal structure of the shock. Any attempt to explain the properties of the electron distribution function using only a piece of the electron distribution function or one-sided information, although useful, is incomplete. To qualitatively determine the types of signatures to expect, the generic formalism is then applied to model electron velocity distribution functions at shocks that have both monotonic and nonmonotonic magnetic fields in section 3 and section 4, respectively. In section 5 the detailed signatures of observed 3-D electron velocity distribution functions within the shock layer are studied in the adiabatic approximation, mapping observed upstream and downstream boundary electron velocity distribution functions to regions inside the shock layer using observed $B(x)$ and $\Phi^{\rm HT}(x)$. Conclusions are presented in section 6.

2. Consequence of $\delta\Phi^{HT} = \kappa\delta B$ on Electron Accessibility

In this paper, unless otherwise noted, we work in the deHoffmann-Teller frame of reference (HTF) because the description of electron energetics and hence change in temperature is much simpler. In solving the steady state electron Vlasov problem in prescribed fields, the issue of electron accessibility is important for two reasons: (1) the determination of the regions of phase space that require specification in order for the problem to be well posed, and (2) solving the Vlasov equation via the method of characteristics once the boundaries have been specified. The boundary conditions once appropriately specified give rise to a unique solution to the Vlasov equation via characteristics throughout the shock layer proper. Whether the solution is consistent with the shock system under consideration depends critically on the chosen boundary condition. Electron accessibility can be determined from the electron energy and magnetic moment constraints specialized to the HTF:

$$E = \frac{1}{2}m_e\left(v_\perp{}^2(x) + v_\parallel{}^2(x)\right) - e\Phi^{HT}(x) = \text{const} \quad (1)$$

$$\mu = \frac{\frac{1}{2}m_e v_\perp{}^2(x)}{B(x)} = \text{const}, \quad (2)$$

where $v_\perp(x)$ and $v_\parallel(x)$ are the local components of the HTF velocity of the electrons perpendicular and parallel, respectively, to the magnetic field. In the unsimplified problem electron accessibility depends on the functional relationship between the magnetic field and the electrostatic potential. In this paper, we assume that the incremental changes in the HTF potential $\delta\Phi^{HT}$ are proportional to the incremental changes in the magnetic field intensity δB through the shock, which is an approximation motivated by theory [*Alfvén and Fälthammer*, 1963; *Whipple*, 1977] and observations [*Hull et al.*, 2000]. The relation between $\delta\Phi^{HT}$ and δB has a simple physical interpretation, namely, the tension between electron mirroring and the desire for the plasma to remain quasi-neutral, with zero current along the shock normal required for time stationary shock layers [*Hull et al.*, 2000]. Zero normal current requires the normal number flux between electrons and ions to be equal. The spatial scale that characterizes the shock magnetic ramp has been observed to be intermediate between the typical electron and ion gyroradii [e.g., *Scudder et al.*, 1986b]. Consequentially, electron behavior is constrained by the first adiabatic invariant, and the electrons remain magnetized throughout the layer. The ions, on the other hand, are demagnetized. The increasing shock magnetic field has a tendency to mirror the magnetized electrons, while most of the ions (a small percentage get specularly reflected), because of their large gyroradii, tend to stream across the layer. The net result of the different inertial responses of the electrons and ions to the shock field structure is an electric field, which acts as a feedback mechanism that

counters electron mirroring and accelerates most of the electrons through the shock so as to maintain a steady state of equal electron and ion normal number fluxes. Thus increases in the HTF potential accompany increases in the magnetic field intensity. Otherwise a normal current would develop, and the shock would not be stationary. *Hull and Scudder* [2000] demonstrated theoretically and from observations that the proportionality constant κ scales as the magnetic moment per unit charge of a typical thermal electron $kT_{e\perp 1}/eB_1$, with the most probable observed ratio $\kappa/(kT_{e\perp 1}/eB_1)$ being 3.0, suggesting that roughly $[1 - \exp(-3)] \sim .95$ of the thermal electrons must get through in order for the electron and ion normal number fluxes to be equal.

Under the assumption of $\delta\Phi^{HT} \propto \delta B$, the determination of electron accessibility from the boundaries that define the system to any point in the shock layer is drastically simplified. For a general shock magnetic field, electrons that have access from some point x' to some other point x'' need to have enough parallel kinetic energy to circumvent the largest potential barrier between x' and x'' (i.e., $\varepsilon_\parallel(x) = \frac{1}{2}m_e v_\parallel{}^2(x) \geq 0$ for all x in $[x', x'']$). This is tantamount to the condition that the minimum electron parallel kinetic energy on the interval $[x', x'']$ be such that $\varepsilon_{\parallel\,\min} \geq 0$. Using (1) and (2) under the assumption that $\delta\Phi^{HT} = \kappa\delta B$, the kinetic energy of an electron parallel to the magnetic field vector $\varepsilon_\parallel = \frac{1}{2}m_e v_\parallel{}^2(x)$ can be written

$$\varepsilon_\parallel(x) = \varepsilon_\parallel(x') + \mathcal{U}_{eq}(x, x'), \quad (3)$$

where the μ dependent change in the equivalent potential energy from x' to x in $[x', x'']$ is given by

$$\mathcal{U}_{eq}(x, x') = \mu\left[B(x') - B(x)\right] - e\left[\Phi^{HT}(x') - \Phi^{HT}(x)\right] = (\mu - e\kappa)\left[B(x') - B(x)\right]. \quad (4)$$

The minimum electron parallel kinetic energy $\varepsilon_{\parallel\,\min}$ is determined from the derivative of (3) with respect to x, which is given by

$$\frac{d\varepsilon_\parallel}{dx} = \frac{d\mathcal{U}_{eq}}{dx} = -(\mu - e\kappa)\frac{dB}{dx}. \quad (5)$$

Thus $\varepsilon_{\parallel\,\min}$ coincides with the minimum in $\mathcal{U}_{eq}$ and is determined from either the maximum or minimum of B depending on the relative size of μ with respect to κ. When $\mu > e\kappa$ the maximum magnetic field amplitude $B_{\max}$ determines $\varepsilon_{\parallel\,\min}$ as follows:

$$\varepsilon_{\parallel\,\min} = \varepsilon_\parallel(x') + (\mu - e\kappa)\left[B(x') - B_{\max}\right] \geq 0. \quad (6)$$

With strict equality (6) defines a modified loss-cone separatrix

$$\alpha_*^2 v_\perp{}^2(x') - v_\parallel{}^2(x') = \frac{2e\kappa}{m_e}\alpha_*^2 B(x'), \quad (7)$$

where $\alpha_*^2 \equiv [B_{\max} - B(x')]/B(x') \geq 0$. Equation (7) partitions $v_\parallel$-$v_\perp$ space at x' into a region which has

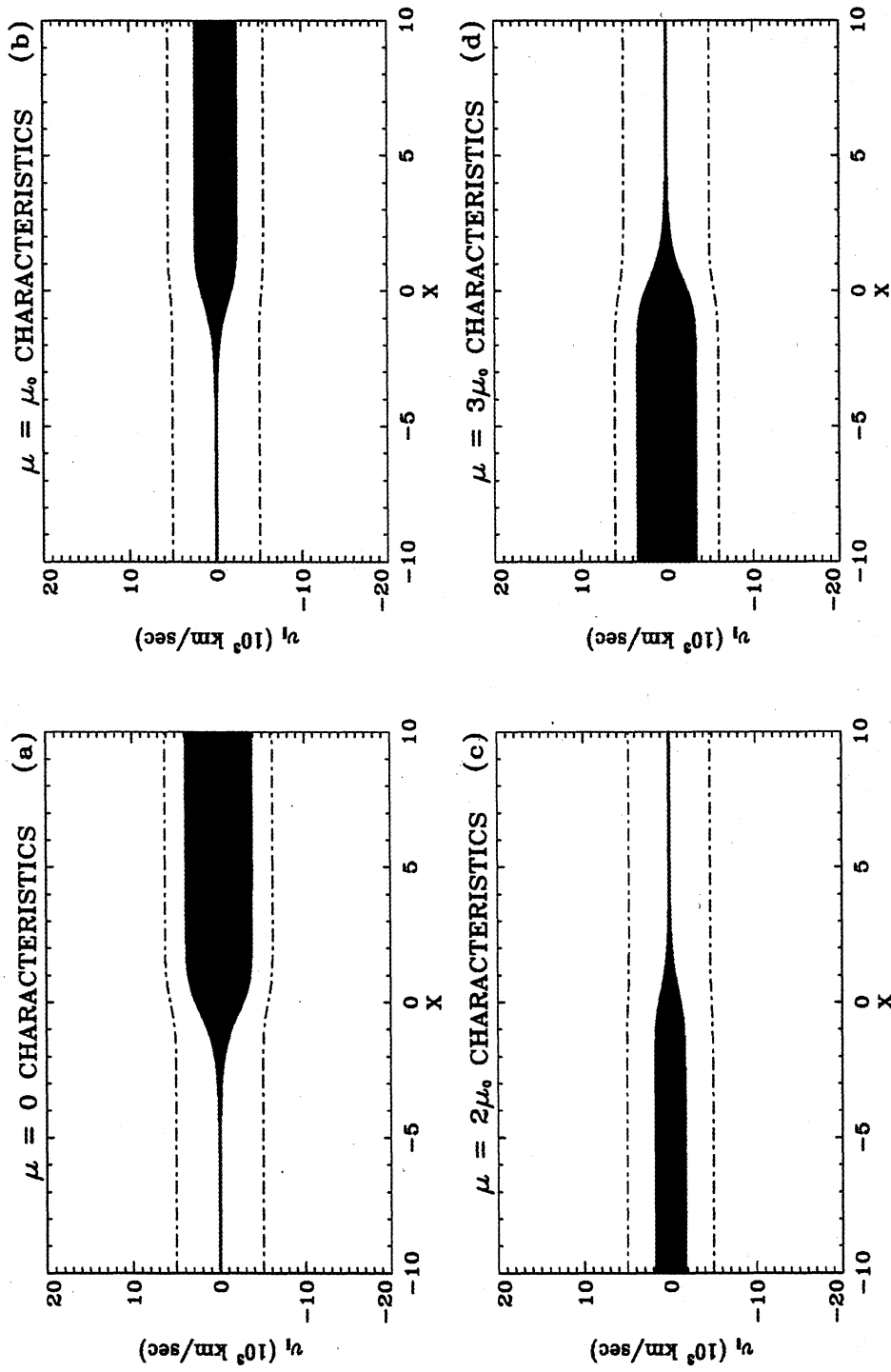**Plate 1.** The topology of characteristics in $X - v_{\parallel}$ space for electrons with (a) $\mu = 0$, (b) $\mu = \mu_0$, (c) $\mu = 2\mu_0$, and (d) $\mu = 3\mu_0$, in a shock layer with a monotonic magnetic field profile.
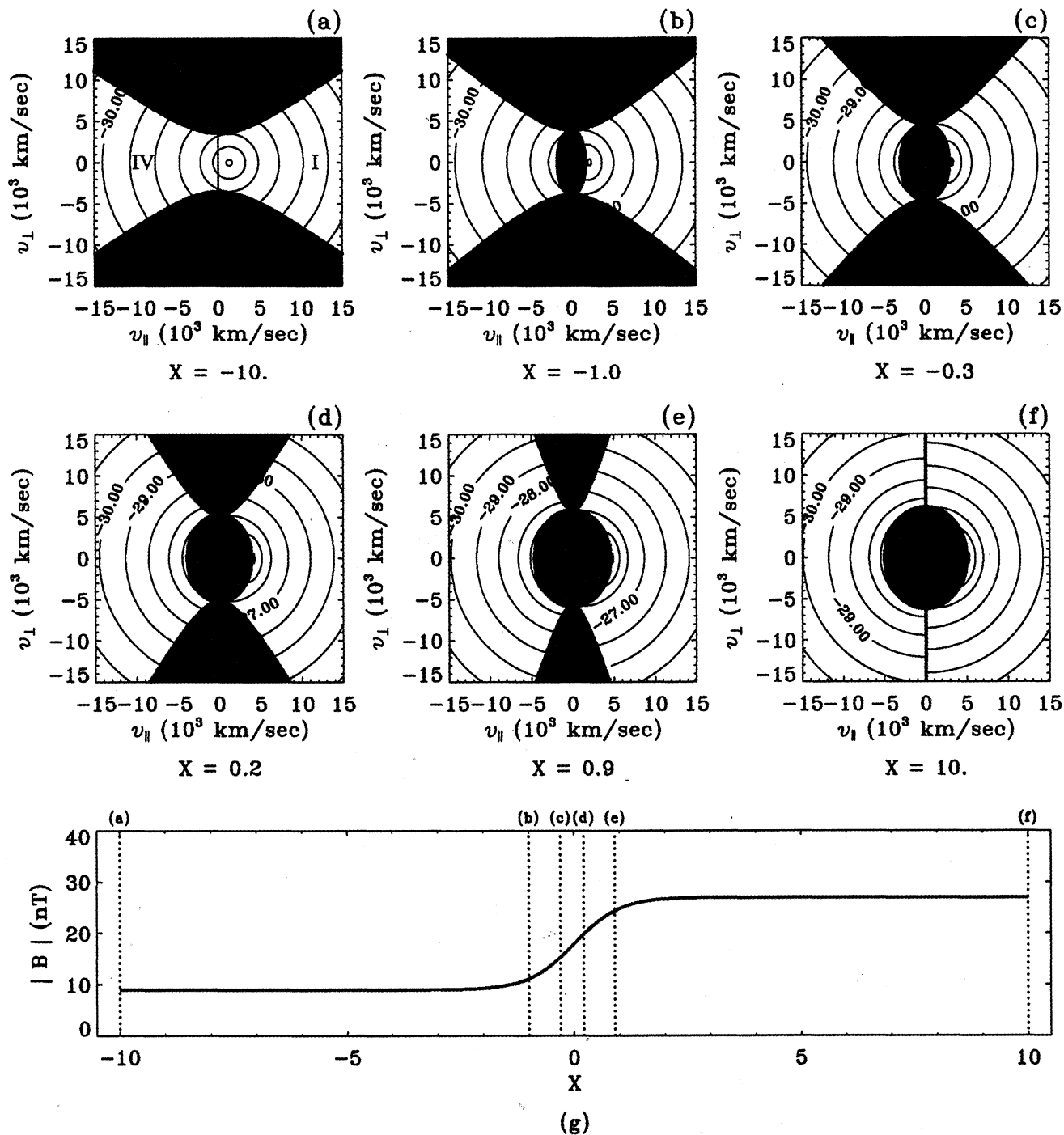
Plate 2. (a)-(f) Level curves of $\log_{10}(f_e)$ (with f_e in cgs units) in $v_\parallel - v_\perp$ space at different locations of the model shock. Plates 2a–2f are color coded in the same format as Plates 1a–1f to indicate the different classes of electron orbits. The model shock magnetic field profile is given in Plate 2g.
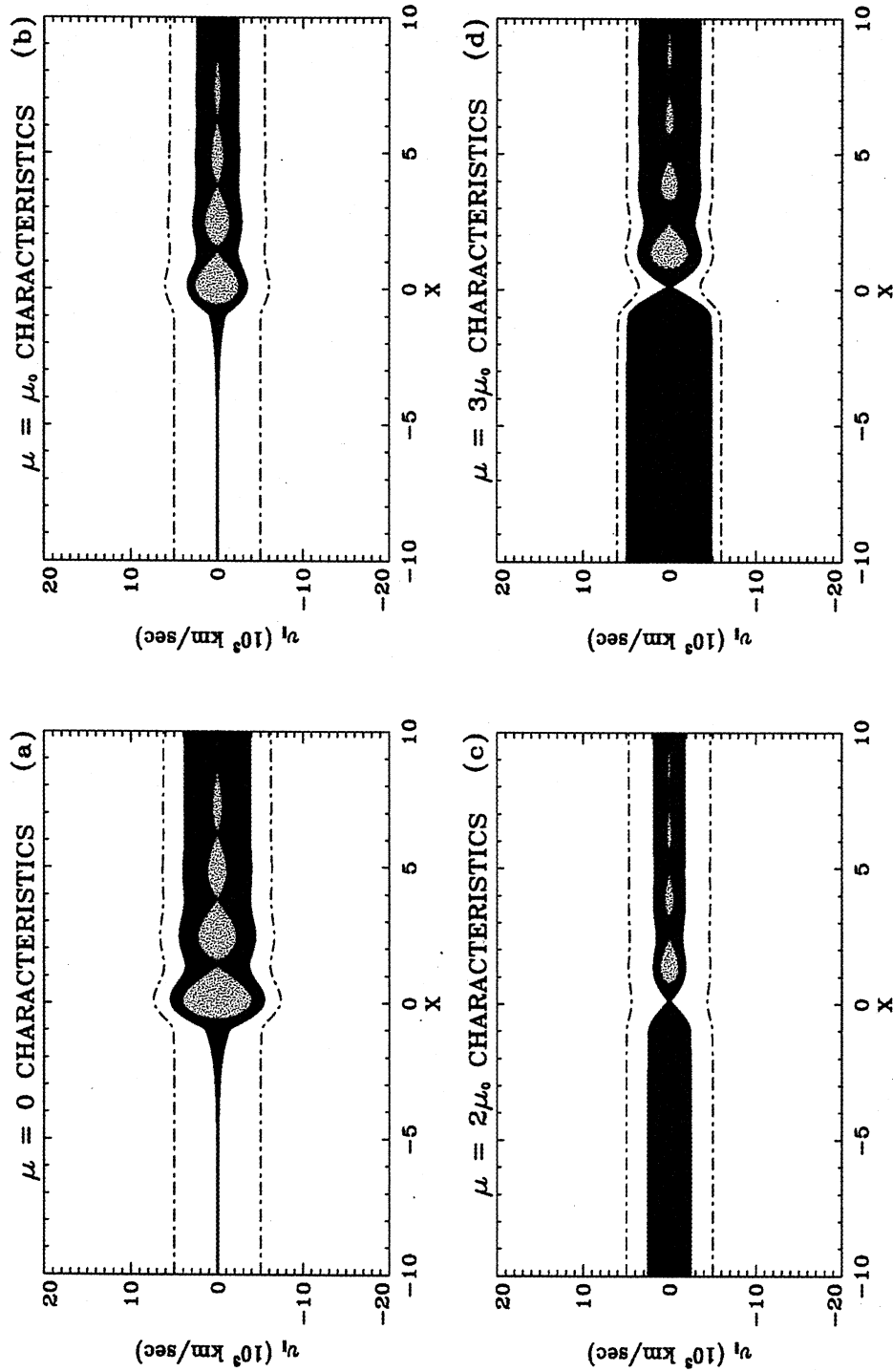
Plate 3. The topology of characteristics in $X - v_{\parallel}$ space for electrons with (a) $\mu = 0$, (b) $\mu = \mu_0$, (c) $\mu = 2\mu_0$, and (d) $\mu = 3\mu_0$, in a shock layer with a nonmonotonic magnetic field profile.

characteristics that connect to x'' and a region with characteristics that do not. In a manner similar to that encountered in studies of the auroral region [*Knight*, 1973; *Whipple*, 1977], the modified loss-cone type of access at collisionless shock layers is controlled by the parallel electric field. Fast mode shocks are characterized by increasing magnetic fields which can reflect electrons trying to make it across the magnetic bottle. However, the parallel electric field is of a sense to counter electron mirroring and accelerates enough electrons through the layer so that the net current is guaranteed to vanish on the downstream side of the shock.

Similarly, when $\mu \leq e\kappa$ the minimum field strength $B_{\min}$ determines $\varepsilon_{\parallel \min}$ as follows:

$$\varepsilon_{\parallel \min} = \varepsilon_{\parallel}(x') + (\mu - e\kappa)\Big[B(x') - B_{\min}\Big] \geq 0. \quad (8)$$

Equation (8) when set to zero results in an ellipsoidal separatrix boundary given by

$$v_{\parallel}^2(x') + \beta_*^2 v_{\perp}^2 = \frac{2e\kappa}{m_e}\beta_*^2 B(x'), \quad (9)$$

where $\beta_*^2 = [B(x') - B_{\min}]/B(x') \geq 0$. Equations (7) and (9) are completely general and can be used to determine the different classes of electron orbits that define $v_{\parallel}$-$v_{\perp}$ space at any point x' in the shock, including the boundaries. In the next two sections the interpretation of the separatrices and consequences on electron phase space topology are discussed in the context of model monotonic and nonmonotonic shock magnetic field profiles.

3. Electron Phase Space Topology: Monotonic Magnetic Fields

In this section electron phase space topology at a shock with a monotonically increasing magnetic field intensity profile under the assumption that $\delta\Phi^{HT} = \kappa\delta B$ is discussed. The phase space topology as determined from (7) and (9) is rather simple at shocks with monotonic magnetic field profiles because there are no trapped electron orbits, for example, electron orbits inside the shock layer map to either the upstream or the downstream spatial boundary. For illustrative purposes we employ a simple model monotonic magnetic field profile generated by

$$B(x) = B_1 + \frac{(B_2 - B_1)}{2}\Big[1 + \tanh\frac{x}{x_0}\Big], \quad (10)$$

where B_1 and B_2 represent the upstream and downstream magnetic field strength, the values of which were chosen to be 5 and 15 nT, respectively. The value of κ, which allows the determination of $\Phi^{HT}(x)$ from (10), was chosen to be 4 V nT^{-1}.

Example equivalent potential energy profiles as seen by upstream electrons with $\mu = 0$, $\mu = \mu_0$, $\mu = 2\mu_0$ and $\mu = 3\mu_0$ ($\mu_0 = m_e V_{\text{th e1}}^2/2B_1 = 2.4$ eV nT^{-1}) at

the idealized shock layer are depicted in Figure 1. The dashed line in Figure 1 indicates where $\mu = e\kappa$. The equivalent potential energy profiles are the result of the competing effects of the accelerating electrostatic field and electron mirroring associated with the increasing magnetic field. Depending on their initial speed and pitch angle, electrons with origins on the upstream side of the shock either traverse the shock layer or get mirrored by the magnetic field during their encounter with the shock layer. Figure 1 suggests that for $\mu < e\kappa$ all upstream electrons with upstream $\varepsilon_{\parallel 1} > 0$ will get accelerated through the monotonic shock potential barrier. When $\mu > e\kappa$ only upstream electrons with $\varepsilon_{\parallel 1} \geq -(\mu - e\kappa)\Big[B_1 - B_2\Big]$ will make it through the shock potential barrier; the rest get reflected at some point in the layer by the magnetic mirror force. The downstream accessibility to the upstream side is similarly determined. Electrons traversing the shock layer from the downstream side of the shock get slowed down by the decelerating parallel electric field and accelerated by the magnetic mirror force. The dashed arrows in Figure 1 indicate the different possible classes of electron orbits.

Plates 1a–1d show the topology of characteristics in $X - v_{\parallel}$ space expected at stationary, fast mode shocks with monotonic magnetic field profiles for electrons with $\mu = 0$ (Plate 1a), $\mu = \mu_0$ (Plate 1b), $\mu = 2\mu_0$ (Plate 1c), and $\mu = 3\mu_0$ (Plate 1d). Example characteristics representing electron trajectories that have access to both boundaries are indicated by the dash-dotted curves in the unshaded regions of $X - v_{\parallel}$ space in Plates 1a–1d. The green regions in Plates 1c and 1d correspond to regions of $X - v_{\parallel}$ space containing electron orbits with origins on the upstream boundary that get reflected by the magnetic mirror force. The dotted curves in the green regions represent typical electron trajectories that get reflected back to the upstream boundary. The blue regions in Plates 1a and 1b are regions of $X - v_{\parallel}$ space containing electron orbits with origins on the downstream boundary that get turned back by the decelerating parallel electric field. Typical electron trajectories reflected back to the downstream boundary are indicated by the dotted curves in Plates 1a and 1b.

To qualitatively illustrate the effects of the shock macroscopic forces on the shape of the electron distribution function across shocks with monotonic magnetic fields, we employed Liouville's theorem to map, along electron characteristic curves, model upstream and downstream boundary distribution functions to regions inside the shock layer. The Vlasov-Liouville mapping approach used in this study is similar that employed in earlier studies [e.g., *Scudder et al.*, 1986c; *Scudder*, 1995; *Hull et al.*, 1998; *Hull and Scudder*, 2000]. Examples of the boundary f_e and resulting V-L mapped electron distribution functions in $v_{\parallel} - v_{\perp}$ space at different spatial locations of the model shock are illustrated in Plates 2a–2f. The model magnetic field
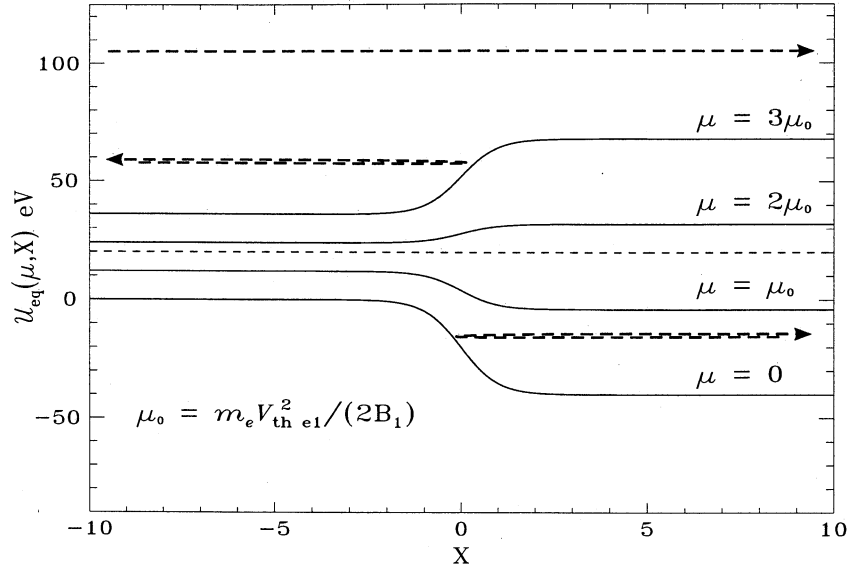
Figure 1. Equivalent potential profiles as seen by electrons with $\mu = 0$, $\mu = \mu_0$, $\mu = 2\mu_0$, and $\mu = 3\mu_0$, at a shock layer with a monotonic magnetic field profile.

profile is depicted in Plate 2g. The location of each distribution function is indicated by the vertical lines. The color, identical to that used in Plates 1a–1d, indicates the different classes of electron orbits. The separatrices that partition $v_\parallel - v_\perp$ space into regions corresponding to different classes of particle orbits indicated in Plates 1a–1d are easily determined from (7) and (9). At the upstream boundary, $B(x') = B_1$, $B_{\min} = B_1$ and $B_{\max} = B_2$ in (7) and (9). The modified loss-cone separatrix (see Plate 2a) determined by (7) is given by the familiar form [e.g., *Scudder*, 1995; *Hull et al.*, 1998]:

$$\alpha^2 v_{\perp 1}^2 - v_{\parallel 1}^2 = \frac{2e\kappa}{m_e}\alpha^2 B_1, \qquad (11)$$

where $\alpha = B_2 - B_1/B_1$. The throat of the separatrix is obtained by setting $v_{\parallel 1} = 0$, which yields

$$v_{\perp 1}^* = \sqrt{\frac{2e\kappa}{m_e}B_1} = \sqrt{\frac{2e}{m_e}B_1\frac{(\Phi_2^{HT} - \Phi_1^{HT})}{(B_2 - B_1)}}. \qquad (12)$$

There is no elliptical separatrix in the upstream $v_\parallel - v_\perp$ space since $B(x') = B_{\min} = B_1$ in (9). Following *Hull et al.* [1998], we adopted the following self-consistent functional form:

$$f_1(\mathbf{v_1}) \equiv \begin{cases} f_{ch}(v_{1\parallel}, v_{1\perp}) & \text{region I} \\ f_{ch}(v_{1\parallel}, v_{1\perp}) & \text{region II} \\ f_{ch}(-v_{1\parallel}, v_{1\perp}) & \text{region III} \\ f_{ch}(v_{1\parallel}, v_{1\perp}) & \text{region IV} \end{cases} \qquad (13)$$

as the upstream boundary distribution function, where the empirically motivated solar wind distribution used to construct $f_1(\mathbf{v_1})$ is the core-halo model given by [*Feldman et al.*, 1975]

$$f_{ch}(\mathbf{v_1}) = \frac{\eta(1-\delta)}{(\sqrt{\pi})^3 \omega_\parallel \omega_\perp^2} \exp\left(-\frac{(v_{1\parallel} - \psi_c)^2}{\omega_\parallel^2} - \frac{v_{1\perp}^2}{\omega_\perp^2}\right)$$
$$+ \frac{\eta\delta}{(\gamma\sqrt{\pi})^3 \omega_\parallel \omega_\perp^2} \exp\left(-\frac{(v_{1\parallel} - \psi_h)^2}{\gamma^2\omega_\parallel^2} - \frac{v_{1\perp}^2}{\gamma^2\omega_\perp^2}\right). \qquad (14)$$

In (14), δ controls the halo density fraction and $\gamma^2 = T_h/T_c$ controls the halo-core temperature ratio. The shape parameters η, $\omega_\parallel$, $\omega_\perp$, ψ_c, and ψ_h determine the total density, core parallel thermal speed, core perpendicular thermal speed, and HTF parallel bulk speeds of the core and halo populations of f_{ch}, respectively. We chose values for η, $\omega_\parallel$, $\omega_\perp$, ψ_c, and ψ_h so that the density, bulk speed, and temperature as defined by the moments of $f_1(\mathbf{v_1})$ represent typical upstream solar wind conditions.

At the downstream $v_\parallel - v_\perp$ space shown in Plate 2f, $B(x') = B_2$ in (7) and (9). Only an elliptical separatrix exists, given by

$$v_{\parallel 2}^2 + \beta^2 v_{\perp 2}^2 = \frac{2e\kappa}{m_e}\beta^2 B_2, \qquad (15)$$

where $\beta^2 = [B_2 - B_1]/B_2$. The elliptical separatrix distinguishes those electrons that communicate with the upstream boundary (unshaded) from those that do not (blue). The electron distribution function in the region of downstream electron velocity space that connects to the upstream boundaries is determined by the upstream boundary condition via Liouville. However, the blue region is a boundary condition that requires specification. The downstream boundary electron velocity distribution function not determined by the upstream distribution function was chosen to be

$$f_2(\mathbf{v_2}) = A\left\{1 + \left[\frac{(v_{2\parallel} - \psi)^2}{\omega_\parallel^2} + \frac{v_{2\perp}^2}{\omega_\perp^2}\right]^q\right\}^{-\nu}, \qquad (16)$$

which is based on fits to downstream electron distribution functions measured by the electron electrostatic analyzer-low (EESA-L) of the three-dimensional plasma (3DP) experiment [Lin et al., 1995] on board Wind. A similar functional form was used by Feldman et al. [1983] to fit 1-D cuts of downstream electron distribution functions measured by ISEE. The parameter q determines the "flatness" of $f_2(\mathbf{v}_2)$ at low energy, whereas ν determines the tails. Typical values for q and ν are 3 and 2, respectively. Values were chosen for the shape parameters A, $\omega_\parallel^2$, and $\omega_\perp$, to represent typical downstream conditions.

Inside the shock layer (Plates 2b–2e) both the modified loss-cone (given by equation (7) with $\alpha_*^2 = [B_2 - B(x')]/B(x')$) and the elliptical separatrix (given by equation (9) with $\beta_*^2 = [B(x') - B_1]/B(x')$) are present. Characteristics within the ellipsoid (blue) can communicate with the downstream boundary but not the upstream boundary. Characteristics outside the hyperboloid of one sheet (green) can communicate with the upstream boundary but not the downstream boundary. Only characteristics outside the ellipsoid and inside the hyperboloid of one sheet (unshaded) can communicate with both boundaries.

In going from the upstream to the downstream side, it is clear from Plates 2a–2f that the macroscopic forces significantly deform and broaden the electron distribution function. The nature of the broadening, as caused by the combined effects of the macroscopic electric and magnetic fields, can be qualitatively inferred from the shape of the elliptical separatrix. In Plate 2b the elliptical separatrix is somewhat "flat," which suggests an anisotropically inflated distribution function. Comparisons between perpendicular and parallel cuts of the distribution depicted in Plate 3b (figure not shown) show that the electron distribution function is preferentially inflated perpendicular to the magnetic field with little or no inflation in the parallel degree of freedom, a property reminiscent of the weak shock transition. With increasing penetration into the shock magnetic ramp, the elliptical separatrix becomes more circular, suggesting a more nearly isotropically broadened electron distribution function on the downstream side of the shock. The region near the peak of the ingoing ($v_{\parallel_1} > 0$) upstream electron distribution function f_1 in Plate 2a gets energized by the parallel electric field, forming a beam in front of the elliptical separatrix in the downstream distribution in Plate 2f. This provides a simple explanation for the formation of electron beams found in the shock transition region and immediately behind the Earth's bow shock [Feldman et al., 1983]. The juxtaposition of ballistically transported electrons from the different sources leads to spatially dependent enhancements/discontinuities in the distribution function organized by the separatrix boundaries. By virtue of the fact that all phase space coordinates inside the shock layer

connect to either the upstream, downstream, or both boundaries means that the electron distribution functions inside the shock layer are completely determined by the upstream and downstream boundary distribution functions. However, in shocks which have nonmonotonic magnetic fields, this is no longer the case, as is discussed in the next section.

4. Electron Phase Space Topology: Nonmonotonic Magnetic Fields

In this section we explore the impact on electron phase space topology of a magnetic field intensity profile with an overshoot magnetic field amplitude $B_{\mathrm{over}} > B_2 > B_1$ under the assumption that $\delta\Phi^{\mathrm{HT}} = \kappa\delta B$. For ease of comparison, the values of B_1, B_2, and κ remain unchanged from the previous section. The model nonmonotonic magnetic field profile in this section was generated by

$$B(x) = \begin{cases} B_1 + \frac{(B_2-B_1)}{2}\left[1 + \tanh\frac{x}{x_0}\right] & x < -x_0 \\ \\ B_1 + \frac{(B_2-B_1)}{2}\left[1 + \tanh\frac{x}{x_0}\right] \\ + c_1 \sin^2[c_2(x + x_0)] \\ \times \exp(c_3|x + x_0|) & x \geq -x_0. \end{cases}$$

(17)

The values c_1, c_2, and c_3 were chosen to be 30, 1.3, and -0.6, respectively, to roughly model the overshoot-undershoot structure of the supercritical shock observed by ISEE-1 on November 7, 1977, previously discussed by Scudder et al. [1986a, 1986b, 1986c].

The resulting equivalent potential energy profiles as seen by electrons with $\mu = 0$, $\mu = \mu_0$, $\mu = 2\mu_0$, and $\mu = 3\mu_0$ at the idealized nonmonotonic shock layer are illustrated in Figure 2. The special case of $\mu = e\kappa$ is indicated by the dashed line in Figure 2. The effect of the nonmonotonic profile with an overshoot ($B_{\mathrm{over}} > B_2 > B_1$) is that more electrons will tend to be reflected by the mirror force than would be in the monotonic case, if nothing else is changed. In addition to the classes of particle orbits that are present at monotonic shock layers, the nonmonotonic features of the equivalent potential result in regions of phase space that correspond to electron orbits (if occupied) that cannot access, by time-independent processes, either the upstream or downstream boundary of the supposed 1-D shock system.

In a format similar to that used in the monotonic case, the characteristic topology in $X - v_\parallel$ space expected at the model nonmonotonic shock magnetic field profile for electrons with $\mu = 0$, $\mu = \mu_0$, $\mu = 2\mu_0$ and $\mu = 3\mu_0$ are given in Plates 3a–3d, respectively. The green regions represent electron orbits with origins on the upstream side of the shock that get reflected by the increasing magnetic field; the blue regions rep-
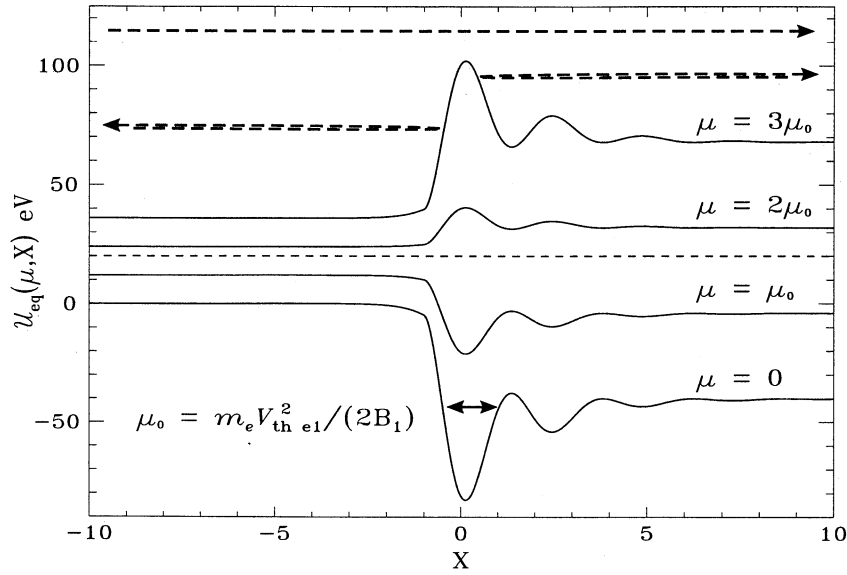
Figure 2. Equivalent potential profiles as seen by electrons with $\mu = 0$, $\mu = \mu_0$, $\mu = 2\mu_0$, and $\mu = 3\mu_0$, at a shock layer with a nonmonotonic magnetic field profile.

resent downstream electrons that get reflected by the electrostatic potential; the unshaded regions represent solar wind ($v_{\parallel} > 0$) and magnetosheath ($v_{\parallel} < 0$) electrons that eventually traverse the shock layer. Typical electron trajectories for each of these regions are shown in Plates 3a–3d. The regions shaded grey represent closed (trapped) electron orbits. These regions, not present in the monotonic example, are outside the domain of 1-D steady state Vlasov as defined by the upstream and downstream boundaries under the assumption $\delta\Phi^{HT} \propto \delta B$. *Scudder et al.* [1986c] discussed the morphology of trapped electron regions in the $\mu = 0$ case. It is clear from Plates 3a–3d that the trapped electron regions persist at all values of μ.

Contour plots of the $v_{\parallel} - v_{\perp}$ space boundary electron distribution functions along with V-L mapped distributions at different spatial locations within the model shock are illustrated in Plates 4a–4f. The vertical lines in Plate 4g indicate where in the idealized shock the electron distribution functions in Plates 4a–4f were sampled. The plots are color-coded in the same manner as Plates 3a–3d, providing a complementary view of the electron characteristic topology through the shock layer. The upstream electron distribution function depicted in Plate 4a is similar to its monotonic counterpart in Plate 2a, although the modified loss-cone separatrix has been qualitatively changed by the magnetic overshoot to the form given by

$$\alpha^2\varsigma^2 v_{\perp 1}^2 - v_{\parallel 1}^2 = \frac{2e\kappa}{m_e}\alpha^2\varsigma^2 B_1, \qquad (18)$$

where the overshoot quantity ς^2 is defined by the expression

$$\varsigma^2 \equiv \frac{B_{\text{over}} - B_1}{B_2 - B_1}. \qquad (19)$$

For fixed κ the throat of the separatrix obtained by setting $v_{\parallel 1} = 0$ is the same in the monotonic and nonmonotonic cases. However, the modified loss-cone cylinder in the nonmonotonic case is flatter than that of the monotonic case as measured by the hyperbola eccentricity:

$$\epsilon_{\text{non}} \equiv \sqrt{\frac{B_{\text{over}}}{B_1}} > \epsilon_{\text{monotonic}} \equiv \sqrt{\frac{B_2}{B_1}}. \qquad (20)$$

Thus, when $B_{\text{over}} > B_2$ a larger volume of the incident electron phase space gets mirrored by the magnetic field, all other things being equal. However, it is important to note that electron acceleration is also enhanced by virtue of the $\delta\Phi^{HT} \propto \delta B$ relationship and thus the modified loss cone throat is enhanced for particle transmission to the high-density side so as to maintain flux balance along the shock normal.

The downstream boundary electron distribution function depicted in Plate 4f is somewhat more complicated than its monotonic counterpart. The same elliptical separatrix, as determined from (15), is present in the $v_{\parallel} - v_{\perp}$ space shown in Plate 2f. However, because of the magnetic overshoot, there exists an additional (blue) region of downstream $v_{\parallel} - v_{\perp}$ space determined by (7) with $\alpha_* = [B_{\text{over}} - B_2]/B_2$ that cannot communicate with the upstream boundary. Electrons in this new exclusion region of downstream phase space near $v_{\parallel} = 0$ eventually get reflected by the magnetic mirror force of the magnetic overshoot analogous to the reflection of electrons incident from the upstream side. The unshaded region in Plate 2f is determined by the upstream condition. A properly posed Vlasov treatment requires specification of the electron distribution function in the blue-shaded region. For the purpose of the Liouville mapping, we used (16) to specify functional form of f_e in this region of downstream phase space.
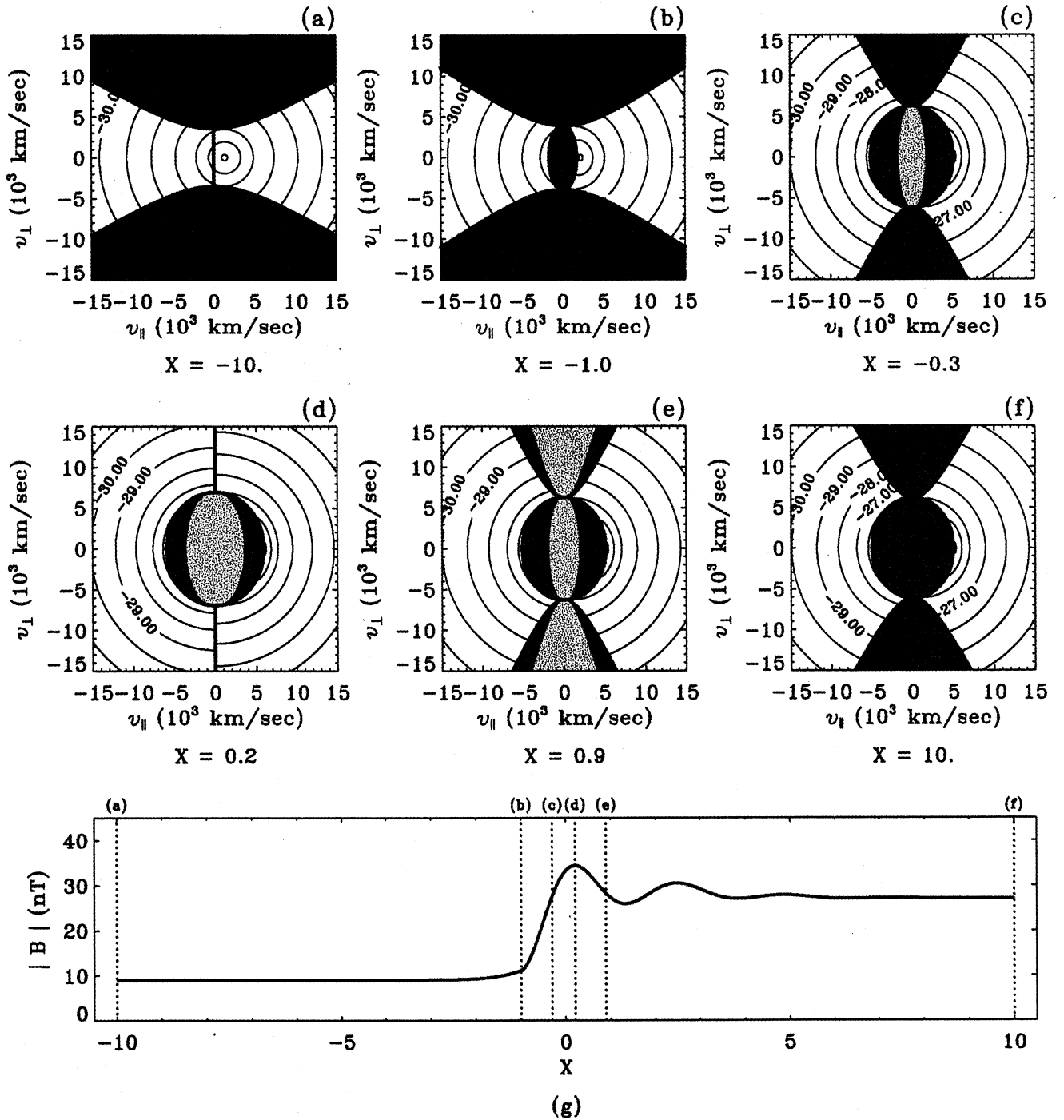
Plate 4. (a)-(f) Level curves of $\log_{10}(f_e)$ (with f_e in cgs units) in $v_\parallel - v_\perp$ space at different locations of the model shock. Plates 4a–4f are color coded in the same format as Plates 3a–3f to indicate the different classes of electron orbits. The model nonmonotonic magnetic field profile is given in Plate 4g.
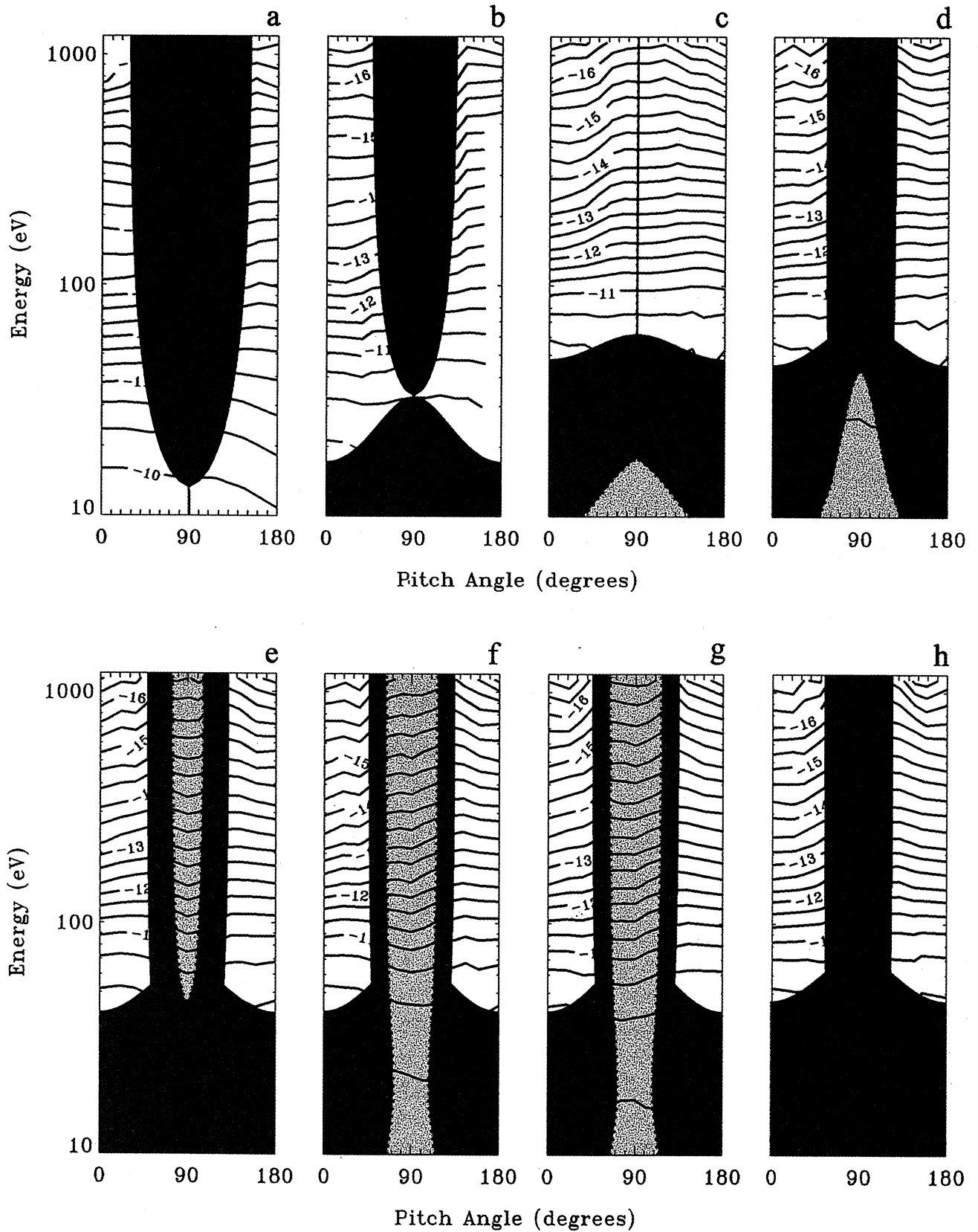
Plate 5. Level curves of the electron distribution function in energy-pitch angle space, sampled at different spatial locations from the upstream to the downstream side of the shock. The color code indicates the different classes of electron orbits.
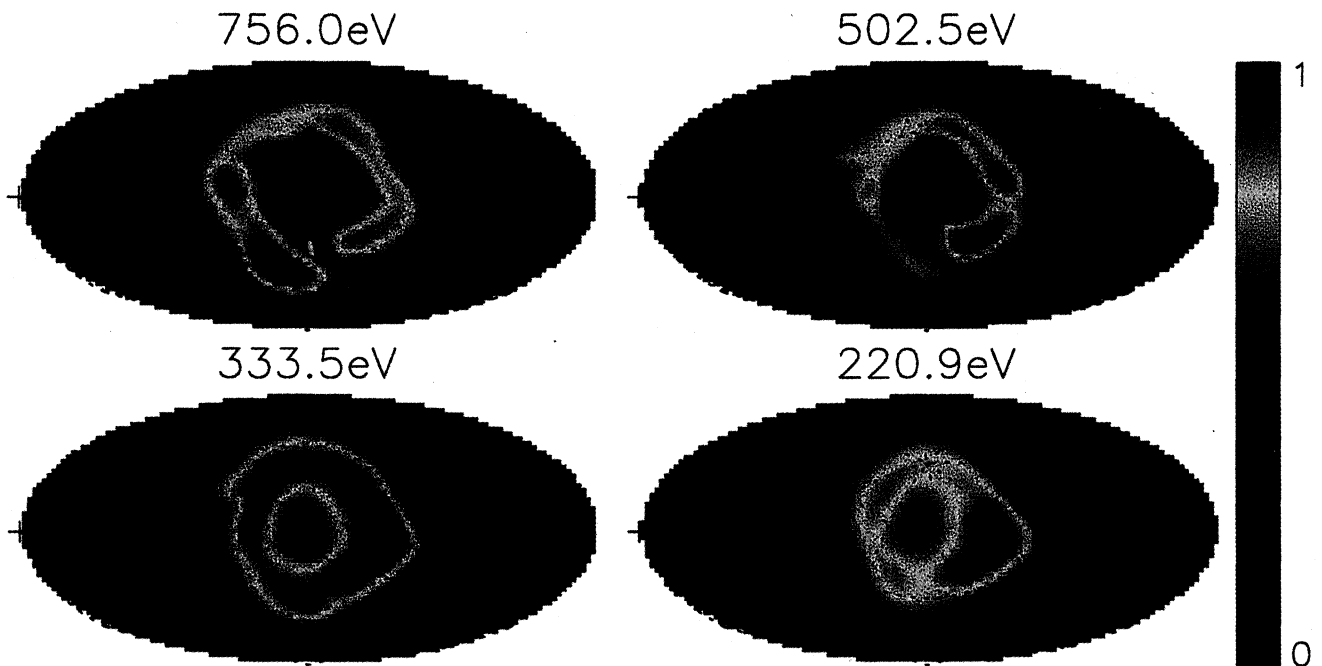
Plate 6. Three-dimensional plots of normalized f_e on a surface of constant energy in the electron rest frame. The solar wind direction is indicated by the asterisks. These plots have been rotated so that the $-\hat{b}$ direction is in the center of each plot (indicated by the diamonds).
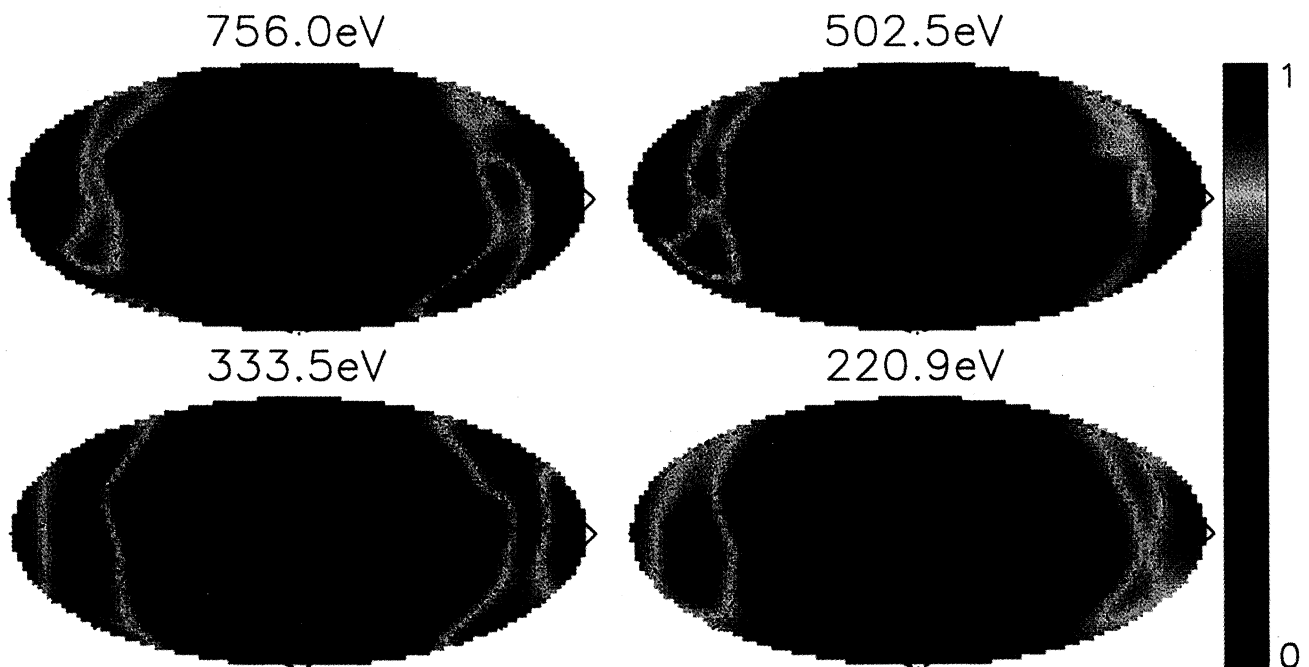

Plate 7. Three-dimensional plots of normalized f_e on a surface of constant energy in the electron rest frame. The solar wind direction is indicated by the asterisks. These plots have been rotated so that the $\hat{b}$ direction is in the center of each plot (indicated by the plus signs).
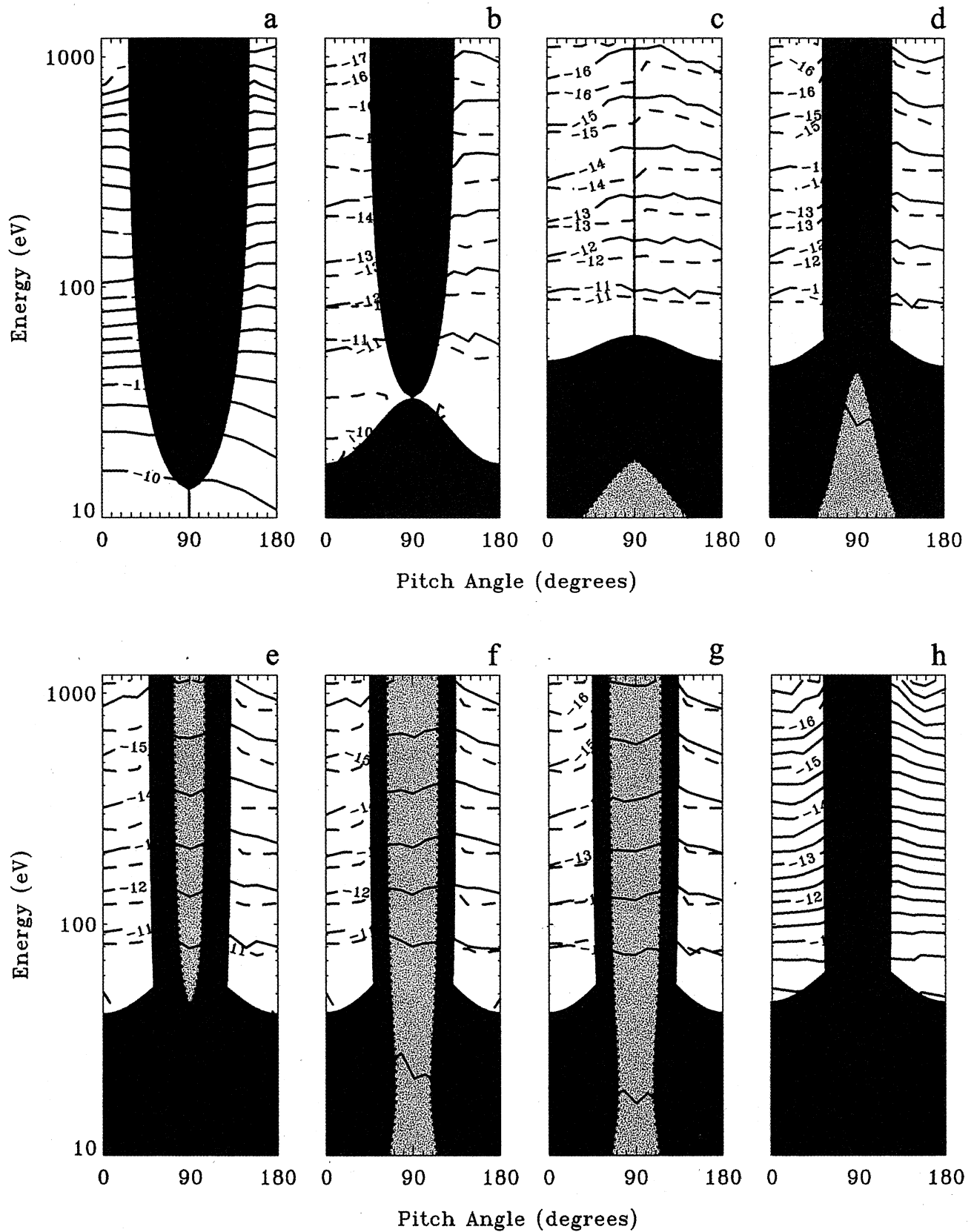
Plate 8. Comparison of the observed electron energy-pitch angle distribution functions (solid contours) at different locations within the shock layer with those predicted by Liouville's theorem (dashed contours).

Inside the shock layer the $v_\parallel - v_\perp$ space can have modified loss cones and elliptical separatrices as determined from (7) and (9) which distinguish transmitted and reflected electron orbits. In addition, there may be modified loss cones and elliptical separatrices as determined from (7) and (9) which distinguish trapped (grey) from untrapped electron orbits (see Plates 4b–4e). The resulting V-L mapped distribution functions inside the shock layer have considerable fine structure depending on the velocity space extent of the trapped region. The distribution in Plate 4b is similar to that depicted in Plate 2b, displaying the preferential perpendicular inflation with little or no inflation parallel to the magnetic field. As in the monotonic example, the peak of the upstream electron distribution function is accelerated by the parallel electric field. However, with increasing penetration into the shock ramp, trapped electron regions at lower energies appear, which occupy a maximum volume of electron velocity space at the magnetic overshoot (see Plates 4c and 4d). There exists exclusion regions at high values of $v_\perp$ near $v_\parallel \sim 0$ immediately behind the shock ramp into the undershoot region (Plate 4e). Consequently, the blue-shaded region of the downstream distribution maps into the narrow blue regions depicted in Plate 4e. The reversible solution is discontinuous at the separatrix boundaries, the strength of which depends on the difference between the phase space densities of the source distributions. Such discontinuities/enhancements, if sufficiently strong, should be present in observed electron distribution functions and therefore can provide important clues to the mechanism or mechanisms responsible for changing the electron temperature across collisionless shocks, in addition to providing clues of the response of the parallel electric field to changes in the magnetic field topology. Given that the exclusion regions are inaccessible to the 1-D adiabatic mapping of upstream and downstream boundary distributions, it is not clear what to expect for the distribution function in these regions of velocity space. Though, if these exclusion regions are not occupied, then the resulting Vlasov predicted electron distribution functions may be unstable [Coroniti et al., 1993; Gedalin, 1999], the properties of which will be dramatically different depending on the spatial location within the shock layer proper. It seems unlikely that these changes provide perturbative corrections to the Vlasov mapping since these trapped regions occupy a significant portion of electron phase space and hence may have a significant effect on the electron moments inside the shock layer. Although the above considerations dealt with prescribed magnetic fields under the empirically motivated assumption that $\delta\Phi^{HT} \propto \delta B$, the results of this section are expected to be topologically similar to cases with a more general relationship between the magnetic field and HTF potential profile.

5. Liouville's Theorem Applied to Observed f_e

Liouville mapped distributions discussed in the previous two sections are of only qualitative merit and are used to illustrate the effects of the shock macroscopic forces and the types of signatures to be expected in the electron distribution function within shocks with monotonic and nonmonotonic magnetic field profiles, respectively. As discussed above, the shock macroscopic electric and magnetic fields impart distinct signatures on the electron distribution function that should be readily seen in observations. The purpose of this section is to establish, from data, aspects of the electron distribution function that can and cannot be explained by the adiabatic motion of electrons across supercritical, fast mode shocks. In this section we analyze the structure of high-time resolution electron distribution functions obtained by the electron electroStatic analyzer-low (EESA-L) of the three-dimensional plasma (3DP) experiment [Lin et al., 1995] as Wind traversed the Earth's bow shock at the GSE (geocentric solar ecliptic) location $\mathbf{X} = (-5.6, 27., -0.2)R_E$ at $\sim$1818:30 UT on July 1, 1998. The electrons were sampled over the energy range from $\sim$10 eV to 1.1 keV in 15 logarithmically spaced energy steps and full 4π angular coverage in one spacecraft spin period (3 s). The EESA-L has an energy resolution $dE/E \sim 30\%$ and angular resolution of roughly $22° \times 22°$. Spacecraft floating potential corrections to the electron measurements were estimated using a least squares fit algorithm to the average photoemission spectrum.

Spin period averaged Wind magnetometer data [Lepping et al., 1995] and high-time resolution (3 s) 3DP moment data measured through the shock are summarized in Figure 3. The data in Figure 3 represent an inbound pass (from the solar wind to the magnetosheath side) of a supercritical, quasi-perpendicular, fast mode shock (the fast mode Mach number $M_{F1} = U_{n1}/C_{F1} \approx 3.0$, where U_{n1} is the upstream relative bulk speed along the shock normal and C_{F1} is the upstream fast mode speed). In addition to UT, the data are given as a function of the downstream convecting ion inertial length $CIIL_2 = U_{n2}/\Omega_{i2}$ (U_{n2} is the downstream normal bulk flow and Ω_{i2} is the downstream ion cyclotron frequency). The plasma moment and magnetic field profiles in Figure 3 are as follows from top to bottom. The top two panels display profiles of the electron (dashed line) and ion (solid line) density and the electron (dashed line) and ion (solid line) bulk speeds, respectively. These panels show the compression ($N_2/N_1 \sim 2.8$) and bulk deceleration of the plasma in traversing the shock layer from the solar wind side to the magnetosheath side of the shock.

The electron (dashed curve) and ion (solid curve)

temperature profiles indicated in the third panel show a relatively strong increase in ion temperature ($\Delta T_i \approx 80$ eV) with a less pronounced electron temperature increase ($\Delta T_e \approx 17$ eV) across the shock. This relationship is consistent with the trends in the observed change in electron and ion temperature featured in earlier studies [e.g., *Schwartz et al.*, 1988]. The electron temperatures perpendicular (dashed curve) and parallel (solid curve) to the magnetic field vector are given in the fourth panel, and the corresponding electron temperature anisotropy $T_{e\parallel}/T_{e\perp}$ is given in the fifth panel of Figure 3. In the solar wind the $T_{e\parallel}/T_{e\perp}$ is greater than unity. In the pedestal region the electron temperature anisotropy becomes less than unity, a transition reminiscent of the weak shock limit, with a preferential increase in $T_{e\perp}$ and little or no change in $T_{e\parallel}$ associated with a slight increase in the magnetic field. With increasing penetration into the shock ramp, $T_{e\parallel}$ begins to increase more rapidly and eventually supersedes $T_{e\perp}$ in the overshoot and undershoot region before relaxing to the level of $T_{e\perp}$ on the downstream side of the shock. The trends in $T_{e\perp}$ and $T_{e\parallel}$ depicted in Figure 3 are typical of a large database of quasi-perpendicular, supercritical Earth bow shock crossings observed by Wind.

The components of the magnetic field vector and the corresponding magnetic field intensity are given in the sixth and seventh panels, respectively, of Figure 3. Typical of a supercritical shock transition, the magnetic field intensity profile is nonmonotonic with a pedestal, overshoot and undershoot region. The asymptotic downstream-upstream magnetic field ratio is $B_2/B_1 = 2.7$. The magnetic field vector is directed into the shock from the solar wind side and is inclined at an angle $\theta_{Bn1} = 78° \pm 2°$ with respect to an inward pointing shock normal $\hat{n}_{VS} = (-0.674, -0.726, 0.137)$ in GSE coordinates, determined via the least squares method of *Viñas and Scudder* [1986] using electron and ion moment data and corresponding spin period resolution magnetic field data. The eighth panel depicts the deHoffmann-Teller frame potential profile $\Phi^{HT}(x)$ computed using electron moment data from the following expression [*Hull et al.*, 2000]:

$$\Phi^{HT}(x'') - \Phi^{HT}(x') = \frac{1}{e}\delta\left[k(\frac{3}{2}T_{e\parallel} + T_{e\perp}) + \frac{q_\parallel}{N_e U_e^{HT}} + \frac{m_e U_e^{HT\,2}}{2}\right], \quad (21)$$

which is derived from the steady state fluid electron energy equation. The δ represents the change in physical parameter, A, in going from some point x' to some other point x'', namely, $\delta A = A(x'') - A(x')$. In (21), $q_\parallel$ is the electron heat flux parallel to the magnetic field vector and $U_e^{HT} = U_{en}/\cos\theta_{Bn}$ is the magnetic field aligned

electron bulk speed in HTF, with U_{en} being the flow velocity along the shock normal. The cross-shock potential jump $\Delta\Phi^{HT}$ is estimated to be 35 eV. The potential increments $\delta\Phi^{HT}$ are proportional to the magnetic field increments δB, as illustrated in Figure 4. The correlation coefficient is $r = 0.87$, and the least squares fit line in Figure 4 has a slope $\kappa = 2.4 \pm 0.3$. The proportionality constant κ_{asympt} that relates the total jump in the HTF potential $\Delta\Phi^{HT}$ to the total change in the magnetic field ΔB is found to be 2.7, which is consistent with the κ determined by the linear fit. Sampling a variety of shock geometries and strengths, *Hull et al.* [2000] found the best correspondence between $\delta\Phi^{HT}$ and δB at shocks characterized by electron $\beta_e \ll 1$, with the correspondence being less accurate at shocks with $\beta_e \gtrsim 1$. The shock event discussed in this paper is characterized by $\beta_e \sim 1.5$. The strong correlation between $\delta\Phi^{HT}$ and δB found in this paper suggests that the equation of state can be extended to shocks with $\beta_e \gtrsim 1$ and that the less accurate correlations given by *Hull et al.* [2000] may be an artifact of the ISEE 1 vector electron spectrometer lower time sampling rates (which at best was 3 second resolution given every 9 seconds). It is not clear whether or not the $\delta\Phi^{HT}$–δB relationship found in this paper or earlier studies can be extended to extremely high Mach number shocks, especially in the limit where the shock ramp becomes thin compared to the typical electron gyroradius. It is our view that the relation between $\delta\Phi^{HT}$ and δB is intimately connected with the adiabatic behavior of electrons in increasing magnetic fields, as discussed above. The nature of the electric feedback is expected to change in the thin shock limit, where most of the electrons and ions are demagetized across the shock. More work, beyond the scope of this paper, needs to be done to establish the validity of the correlation between $\delta\Phi^{HT}$ and δB and its relation to characteristic shock parameters, including high values of β_e and very high Mach numbers. A summary of the shock asymptotic parameters is given in Table 1 as a reference.

Plates 5a–5h portray samples of the electron distribution function in energy-pitch angle (E-α) space measured at the spatial locations indicated by the solid lines in Figure 3. Because high-time-resolution magnetic field data were not available, we used the 3-s resolution magnetic field data to sort each electron distribution measurement into E-α bins, which were then bucket averaged. The electron distribution functions depicted in Plates 5a–5h have been transformed to the HTF. Transformation to the HTF is achieved by converting the coordinate of each distribution measurement to the plasma rest frame and then shifting by the local HTF bulk velocity, which is given by $\mathbf{U}^{HT} = U_n/\cos\theta_{Bn}\hat{b}$. The color code indicates the different classes of electron orbits. The separatrix boundaries depicted in Plates
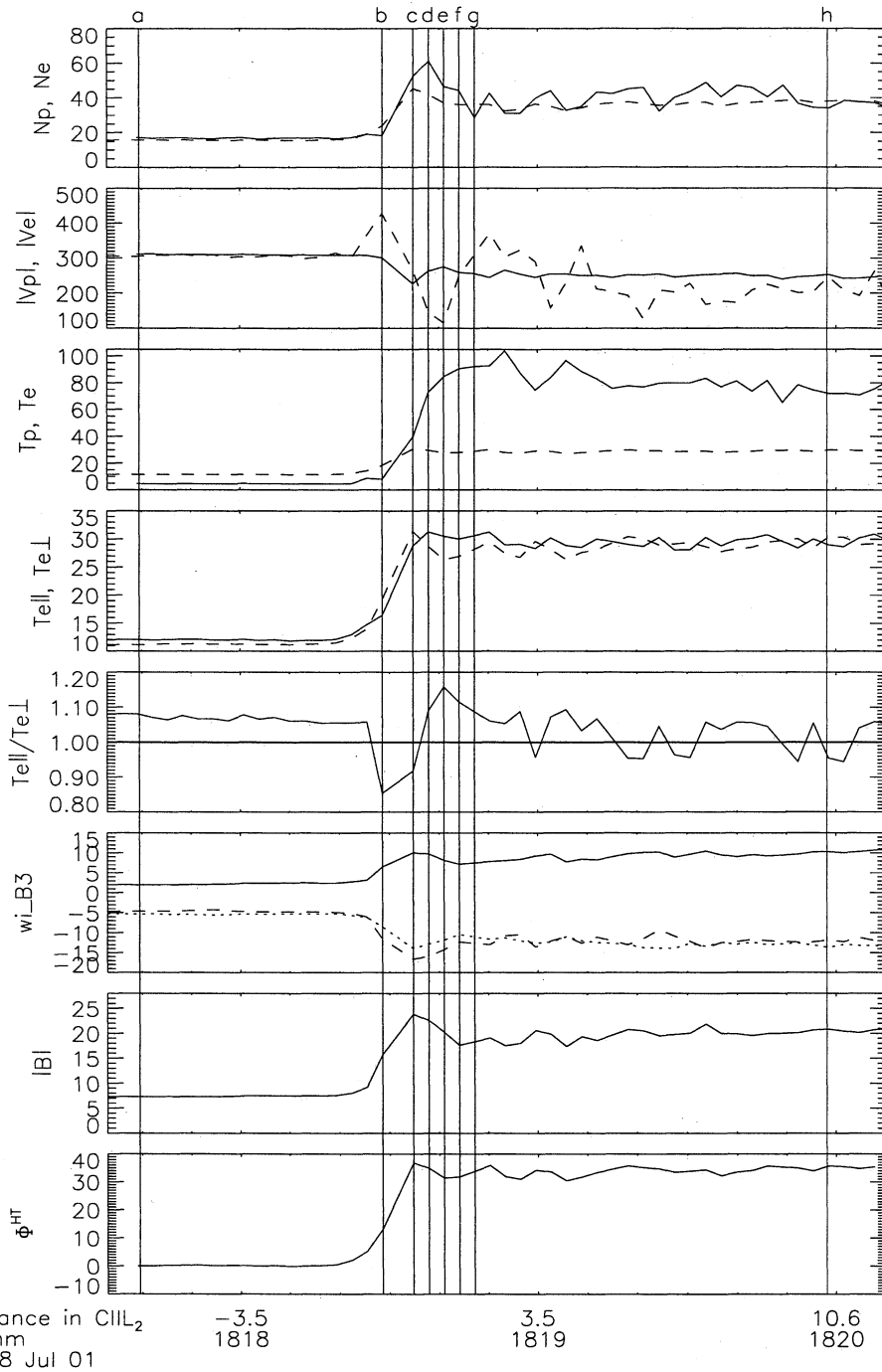
Figure 3. The top two panels depict profiles of the electron (dashed curve) and ion (solid curve) densities and bulk speeds, respectively. The third panel displays the electron (dashed curve) and the ion temperature (solid curve). The electron temperatures perpendicular (dashed curve) and parallel (solid curve) to the magnetic field vector are given in the fourth panel, and the corresponding electron temperature anisotropy $T_{e\parallel}/T_{e\perp}$ is given in the fifth panel. The sixth and seventh panels depict the components of the magnetic field vector and the corresponding magnetic field magnitude, respectively. The eighth panel displays the de Hoffmann-Teller frame potential profile.

5a–5h are determined from measured $B(x)$ and $\Phi^{HT}(x)$, with no assumption on the functional relationship between $B(x)$ and $\Phi^{HT}(x)$. A correspondence between the separatrix boundaries and the signatures of f_e is a necessary, but not sufficient, condition for evidence of the adiabatic behavior of the electrons in the shock dc electric and magnetic fields as predicted by V-L theory.

Plate 5a is the electron distribution function measured just upstream of the shock. The electron distribution function at pitch angles ranging from 0° to 90°
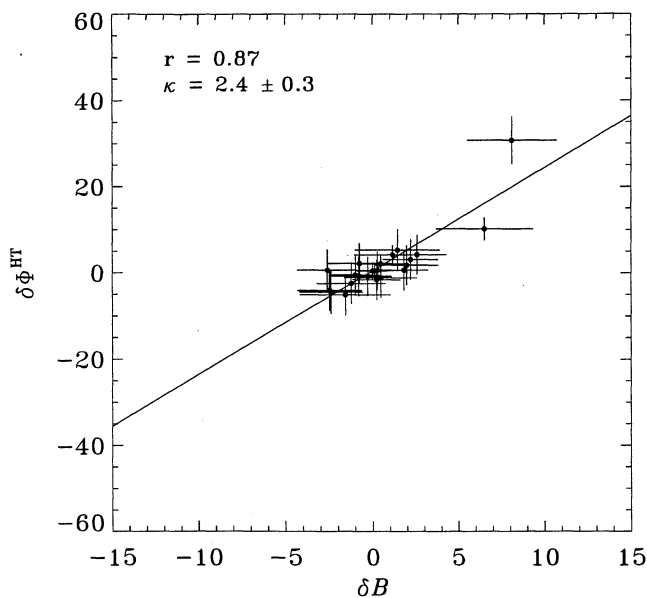
Figure 4. Comparison of the incremental changes in the magnetic field δB with the incremental changes in the deHoffmann-Teller reference frame potential $\delta\Phi^{HT}$ at the Earth's bow shock observed by Wind on July 1, 1998, at ~1818:30 UT.

represents the ingoing upstream electron boundary distribution. The electron distribution in this region of E-α space have no foreknowledge of the impinging shock layer and is well modeled as a convecting core-halo distribution [*Feldman et al.*, 1975]. The unshaded region represents electrons that have access to the downstream boundary. The electrons occupying the green region at pitch angles $< 90°$ get mirrored and eventually compose the electron distribution in the region shaded in green at pitch angles $> 90°$. The outgoing loss-cone electron distribution function (unshaded region at pitch angles $> 90°$) represents magnetosheath (MS) electrons that have leaked into the upstream side of the shock.

There exists a remnant of a discontinuity in the electron distribution function at the junction where the separatrix boundary separates the reflected from the MS electrons, as one should expect for adiabatic electron transport. The magnetosheath electrons are at a higher/lower phase space density than the reflected electrons at higher/lower energies. The enhancements at $\alpha \approx 180°$ may be explained by the free-streaming magnetosheath electrons, which initially determine the ingoing solar wind heat flux, that traverse the shock and then subsequently escape back into the solar wind side along the magnetic field line that intersects the curved bow shock at two points.

The distribution function in the shock ramp (Plate 5b) is slightly inflated and shows signs of the formation of an electron flat-top at lower energies. The blue region estimates particle trajectories that have access to the flat region from the downstream boundary. In the shock magnetic overshoot region (Plate 5c and 5d), the distribution function is substantially broadened, with a preferential enhancement near $\alpha \sim 90°$ at higher energies. The f_e is relatively flat at $E \sim 50$ eV. In the vicinity of the magnetic undershoot (Plates 5e–5g), the electron distribution functions show double peak enhancements at higher energies, near $\alpha = 60°$ and $\alpha = 120°$, respectively. The enhancements are roughly mirror symmetric, although the intensity of the outgoing enhancement appears to be systematically lower than that of the ingoing enhancement. We compared the ingoing and outgoing enhancements and found that they differ, for the most part, by less than 25%. The fact that the intensity of the outgoing enhancement is systematically lower than that of the ingoing enhancement can be explained by errors in transforming to the HTF. In the case of Plate 5e, a 10% correction (≈ 100 km/s) to the HTF transformation velocity significantly reduced the slight systematic asymmetry between the ingoing and outgoing enhancements. Whether or not the enhancements

Table 1. Asymptotic Shock Parameters

Parameter	Upstream	Downstream	Units
Magnetic field intensity, B	7.4 ± 0.3[a]	20.0 ± 1.3[a]	nT
Magnetic field unit vector, GSE, $\hat{b}$	(0.358, -0.729, -0.583)	(0.457, -0.645, -0.613)	
Angle between $\hat{n}$ and $\hat{b}$, θ_{Bn}	$78° \pm 2°$[b]	$86° \pm 2°$[b]	
Plasma density, N	17.0 ± 0.4[a]	48 ± 4[a]	cm^{-3}
Normal bulk speed, U_n	185 ± 8	66 ± 9	km s^{-1}
Electron temperature, T_e	1.4 ± 0.1[a]	3.4 ± 0.1[a]	10^5 K
Ion temperature, T_i	0.50 ± 0.03[a]	8.4 ± 0.5[a]	10^5 K
Electron beta, β_e	1.5	1.4	
Ion beta, β_i	~0.5	~4.0	
Fast mode Mach number, M_f	3.0	0.5	
Alfvén Mach number, M_A	4.7	1.1	
HTF potential jump, $\Delta\Phi^{HT}$	—	35[c]	V

[a] Observations.
[b] Estimated from plasma and field data via the least squares method of *Viñas and Scudder* [1986].
[c] Estimated using the steady state electron energy equation.

are real (e.g., gyrotropic) or the result aliasing is not obvious from Plates 5e–5g. It is important to note that, by construction, the EESA-L detector does not sample counts simultaneously in all directions at once; EESA-L measures all polar angles θ divided into eight bins and finite azimuthal angle ϕ in a given energy sweep time interval and thus requires a full spin period to measure the full 3-D count spectrum. Dramatic changes in the plasma properties occur at the shock. The changes can be so drastic that in the 3 s sampling time (which is much greater than the electron gyroperiod), the resulting measured electron distribution function can be severely aliased and can have distortions/enhancements which are not necessarily gyrotropic in the 3-D image of the distribution function and are therefore not physical. To show that the double peak enhancements are real attributes of the electron distribution function (e.g., not significantly aliased), Plates 6 and 7 depict complementary views of the full 3-D electron distribution function, corresponding to the E-α representation of f_e displayed in Plate 5e. Each panel in Plates 6 and 7 depicts normalized f_e on a surface of constant energy in the electron rest frame. The Hammer-Aitoff equal area projection is used to display 4π sr angular coverage. The solar wind direction is indicated by the asterisk in each of the panels in Plates 6 and 7. Each panel depicted in Plate 6 has been rotated so that the $-\hat{b}$ direction is in the center (indicated by the diamond). Thus the center of each panel provides a view of magnetosheath electrons that are propagating toward the shock, whereas the outer edges of each panel represent a view of magnetosheath electrons that are moving away from the shock. The red ring about the center of each energy panel corresponds to the enhancement near 120° in Plate 5e. Plate 7 depicts the same full 3-D electron distribution function in the same format as Plate 6, except that the distribution measurements at constant energy have been rotated so that the $\hat{b}$ direction is in the center of each panel (indicated by plus signs). The green ring about the center of each panel of Plate 7 corresponds to the enhancement near 60° in Plate 5e. Because the 3 s sampling time corresponds to $\approx$1500 electron gyroperiods, it is not possible to tell from the measurements whether the enhancements in Plate 5e are the result of gyrotropically distributed electrons as required for the V-L interpretation to be valid or the result of gyrophase bunched electrons. However, the results of Plate 6 and Plate 7 demonstrate that gyrotropy is plausible. Moreover, the correspondence between the enhancements and the separatrix boundaries depicted in Plate 5e provides a natural interpretation, namely, the result of gyrotropic, free-streaming magnetosheath electrons propagating toward the shock and their magnetically reflected image in analogy to Plate 4e. On the basis of arguments given in section 4, the grey regions in Plate 5 represent trapped electron components. These

observations suggest that the exclusion regions are occupied.

The downstream electron distribution function is given in Plate 5h. The double peak enhancements of Plates 5e–5g have collapsed to the single peak enhancement about 90° shaded in blue in Plate 5h. The 3-D distribution plots (figure not shown) indicate that this single peak enhancement is consistent with gyrotropy. The separatrix that bounds the enhanced region in Plate 5h suggests that this perpendicular enhancement is the free-streaming source of the enhancements in the electron distribution function displayed in Plate 5d and 5e. In this shock example, we did not see any distinguishable beam signature in the electron distribution inside and downstream of the shock layer as predicted by Vlasov and often found in the observations [e.g., *Feldman et al.*, 1983; *Scudder et al.*, 1986c]. In the study by *Feldman et al.* [1983], the beam signatures, when observed, were most notable in the shock ramp, but the beam decreased in amplitude with increasing penetration into the ramp and eventually merged with the flat-top part of the distribution function on the downstream side of the shock. It may be the case that the rapid variations in the magnetic field in the shock ramp, coupled with the possible rapid erosion of the beam via wave-particle interactions, which are outside the scope of V-L theory, preclude EESA-L from detecting the beam, if it were to initially be present. Considerable variations in the magnetic field direction will have the effect of smoothing the electron distribution in pitch angle. This effect is most drastic within the shock ramp, where the rapidly changing magnetic field gives rise to uncertainties in pitch angle of $\sim$20°.

A survey of electron distribution function data at several shocks with overshoot-undershoot structure showed that the double peak enhancements are typically observed at those shocks characterized by downstream electron distribution functions enhanced near $\alpha \sim 90°$. When the 90° enhancement was not present in the downstream distribution function, the distribution function near the undershoot tended to have a shallow trough near $\alpha \sim 90°$ at higher energies.

It is not enough to show that the electron phase space can be organized by the separatrix boundaries determined by the macroscopic electromagnetic fields to verify the mechanism responsible for the shape of the electron distribution function within the shock layer. Self-consistency requires, within reason, that the electron distribution function should match the free streaming image from the upstream and downstream spatial boundaries that connect to the point of interest within the shock layer. As a simple test, we employed the V-L mapping approach to map observed upstream and downstream boundary electron distribution functions to different spatial locations within the shock. Plates 8b–8g compare, where a correspondence can be made, the

level curves of the observed energy-pitch angle distribution functions (solid contours) with the V-L predictions (dashed contours) at the different spatial locations indicated by the vertical lines in Figure 3. The V-L predictions are determined from the upstream and downstream boundary electron distribution functions depicted in Plate 8a and 8h, respectively. The V-L mapping procedure recovers the lowest order broadening of the electron distribution function throughout the shock layer proper in the regions where the steady state Vlasov theory is valid. Quite remarkable is the fact that the complex signatures of the electron distribution function such as the perpendicular enhancement of the electron distribution function near the overshoot (Plate 8d) and the double peak enhancements of electron distribution functions observed behind the magnetic overshoot (Plates 8e and 8f) are recovered.

Discrepancies between the V-L theory and the observations are difficult to ascertain and can be explained by a number of effects. One possibility is that the shock state may be changing over the time interval (~1.5 min) the single spacecraft (S/C) took to measure electron distribution functions from the upstream to the downstream side of the shock. In this paper we assumed that the shock state is stationary over the upstream-downstream sampling time. However, it is possible for the electron distribution function in the layer to have a slightly different history from the boundary electron distribution functions used to determine the V-L predictions inside the shock layer. Although errors associated with temporal variations in the shock state were minimized by using upstream and downstream boundary distribution functions measured within a few minutes of the shock layer, uncertainties associated with a slightly changing shock state may not be negligible.

Another possibility may be errors introduced in frame transformations. Each individual S/C frame distribution function coordinate was transformed to an equivalent E-α coordinate in HTF using 3-s resolution magnetic field measurements. As mentioned above, small errors in the HTF transformation velocity can introduce systematic asymmetries in the distribution function. Moreover, significant changes in the plasma properties and the magnetic field direction and magnitude during the 3 s accumulation time of f_e can lead to significant uncertainties in the assignment of each distribution function measurement to an E-α coordinate. This aliasing effect is most significant in the shock ramp and probably can explain the significant discrepancies between the V-L predictions and observations in Plate 8b. As mentioned above, the variation in the magnetic field in the ramp accounts for an error of roughly ~20°, leading to an effective angular resolution (detector + field variations) of roughly ~30°. Systematic variations in the plasma density and velocity in the ramp are expected to introduce systematic errors in the electron distribution function, which are more difficult to quantify.

Outside of the magnetic ramp, the magnetic field fluctuations were quite small (e.g., $dB/B \lesssim .1$), accounting for $\lesssim 6°$ error in pitch angle.

The discrepancies between the theory and the observations could also be an artifact of inaccuracies in the determination of the electron orbit. Generally speaking, the adjustment in energy required for exact agreement between the V-L theory and the observations is from 10% to 20%, although in places, as in the transmitted (unshaded) regions of electron phase space, the discrepancy can be as much as 30%. (It is important to note that using the difference between the observed f_e and the corresponding V-L prediction as a measure of success or failure of the theory can be misleading because small departures to the orbit in energy can give rise to significant differences between the theoretical and experimental f_e, especially in the power law tails.) The effects of magnetic field fluctuations and errors in the determination of $\Phi^{HT}(x)$ lead to propagated uncertainties in the mapped electron energy ranging from 15% to 25%, which are commensurate with the shift in energy required to get the theory to agree with the observations, and therefore can account for the departures between the theory and observations. However, the departures in energy appear to be systematic, namely, Vlasov theory tends to overestimate f_e near the edge of the flat-top region and tends to underestimate f_e at higher energies. A similar tendency was found in comparisons between the observed parallel cut of the electron distribution and the Vlasov predictions in the earlier study by *Scudder et al.* [1986c]. It may be the case that the systematic departures at higher energies ($\gtrsim$ few hundred eV) in the transmitted regions (unshaded) of electron phase space are a manifestation of higher-order terms in the guiding center ordered asymptotic series of the electron orbit. The ratio between the electron gyroradius and the scale that characterizes the magnetic field variation $\epsilon = r_\perp/L_B$ determines the relative importance of higher-order corrections to the guiding center orbit. Measurements of the shock fields from two S/C, as in ISEE 1 and ISEE 2, are necessary to get accurate estimates of the relative shock velocities along the shock normal and hence to obtain high-precision estimates of the characteristic shock spatial scales L_B [e.g., *Scudder et al.*, 1986a; *Newbury et al.*, 1998]. For a 1 keV electron in the ramp of the shock, a rough estimate for ϵ is found to be ~0.2, suggesting that the 1 keV electron should be magnetized across the shock ramp. However, more reliable estimates of the shock scales (e.g., high-resolution measurements of the magnetic field by multiple S/C) are required to obtain accurate determinations of ϵ, which in our example can be off by a factor of 2 or more. In order to accurately describe the more energetic component of the transmitted electrons, the mapping may need to be revised to include higher-order corrections to the electron orbit, and potentially nonadiabatic effects (Liouville should still be valid in the

nonadiabatic limit, although μ conservation no longer applies). The details of electron orbits in the transition from the infinitesimal gyroradius regime to the nonadiabatic regime are difficult to quantify from the observations and will not be dealt with further in this paper. Another possible source of the systematic departures between theory and observations at high energy is the 1-D planar symmetry assumed in the V-L model. The 3-D nature of the Earth's bow shock may play a role, although the relative importance of 3-D effects is not clear at this point and is left for future work. Finally, wave-particle effects may not be negligible as has been assumed in the Vlasov model. Despite all of the pitfalls of the measurement process, the V-L procedure does a good job of recovering the salient features of the electron distribution function, providing a good lowest-order approximation of f_e where comparisons can be made.

It is important to note that a large portion (indicated in grey in Plate 8) of electron phase space is outside the 1-D, steady state Vlasov approach as defined by the upstream and downstream boundary conditions. We found that the combined smoothing effects of the angular and energy resolution of the EESA-L detectors and aliasing associated with variations in the magnetic field could not explain the filling of these exclusion regions. Unoccupied regions of electron phase space remain empty after boxcar smoothing the V-L predictions over the effective angular resolution of the detector and magnetic field variations. An outstanding question remains: How do the electrons get into the exclusion regions of electron phase space? At this moment, we can only conjecture about the origins of the electrons in this region of phase space. One possibility is that electrons can get scattered into these regions via waves. Observations of plasma waves [*Gurnett*, 1985] in the shock transition region of quasi-perpendicular shocks have revealed the presence of a rather abrupt broadband burst of electrostatic noise extending below the lower hybrid resonance to near the electron plasma frequency. Broadband bursts of whistler mode electromagnetic noise at frequencies below the electron cyclotron frequency have also been observed [*Gurnett*, 1985]. As an explanation of broadband electrostatic noise observed in a variety of contexts including the Earth's bow shock, *Coroniti et al.* [1993] proposed the nonstandard "hole" modes which occur as the result of a hole at low energies in the electron velocity distribution function. The hole mode, existing only for a narrow range of propagation angles about the magnetic field, has a growth rate that is strongly enhanced if the parallel temperature moderately exceeds the perpendicular temperature, which is the case near the magnetic overshoot and into the undershoot region as suggested by the fifth panel of Figure 3. Recent observations [*Matsumoto et al.*, 1997; *Bale et al.*, 1998] indicate that the electrostatic turbulence is highly nonlinear and often composed of bipolar electric spikes. The intensities of these bipolar spikes have a strong correlation with the change in the electron temperature and are anticorrelated with the plasma beta (S. Bale, personal communication, 1999). These bipolar structures are suggestive of BGK-mode electron phase space holes. Whether these spikes are the result of phase space "voids" at lower energy and possible involvement in irreversible changes to the electron distribution is not well understood. Instabilities in the lower hybrid regime ($\omega \sim \Omega_{LH}$) which include the modified two-stream instability, the kinetic cross-field streaming instability, and the lower hybrid drift instability may play a role [*Winske et al.*, 1985; *Scudder et al.*, 1986c; *Winske et al.*, 1987; *Gedalin*, 1999], though it is still not clear how important these are in heating electrons at collisionless shocks. It is important to note that significant wave particle modification of the exclusion regions does not preclude an adiabatic description for f_e elsewhere in velocity space. The regions at the edges of the exclusion regions are where the velocity space gradients are steepest. Wave particle interactions could act in a quasi-linear sense to fill these exclusion regions without affecting f_e much everywhere else. The detailed analysis of Wind wave data for this event and their association with properties of the electron distribution is left for future work. Partial filling/trapping associated with adiabatic access in connection to the 3-D nature of the Earth's bow shock cannot be ruled out.

6. Conclusions

The properties of electron phase space were explored in the context of collisionless shocks with monotonic and nonmonotonic magnetic field profiles under the empirically motivated approximation that $\delta\Phi^{HT} \propto \delta B$ [*Hull et al.*, 2000]. Liouville's theorem was used to map model electron distribution functions across model shock monotonic and nonmonotonic magnetic fields to determine what distribution signatures to expect within the shock layer. We demonstrated that the macroscopic electromagnetic forces significantly deforms and broadens the electron distribution function in both cases, providing a very efficient mechanism for changing the temperature of adiabatic electrons, as they traverse the shock layer. As long as the equivalent potential is monotonic, we argue on the grounds of Liouville's theorem in the adiabatic approximation that the electron distribution function within shocks with monotonic magnetic fields can be completely determined from the ingoing upstream and downstream boundary distribution functions. However, nonmonotonicities in the electric and magnetic fields lead to a nonmonotonic equivalent potential energy profile which may trap electrons. The trapped electron regions encompass the low-energy portion of the electron distribution (which from observations at strong shocks is found to be flat-topped) due to nonmonotonicities in the parallel electric field in addition to regions at higher energies near 90° pitch angles

associated with nonmonotonicities in the shock magnetic field. The qualitative V-L model predicts that electron distribution functions inside shocks with nonmonotonic electromagnetic fields should be composed of free-streaming electrons with solar wind and magnetosheath origins, and possibly trapped electron populations. The juxtaposition of electrons from different sources is expected to give rise to fine structure in the electron distribution function that should be easily identifiable in the experimental data. It is important to note that nonmonotonic magnetic fields also have the secondary effect of increasing the accelerating potential to the highest overshoot, thereby enhancing heating, that for electrons would be limited in the monotonic case by the upstream-downstream field compression.

As a test of the V-L model predictions, we analyzed the detailed signatures of electron energy-pitch angle distribution functions observed at different spatial locations within a fast mode shock characterized by a nonmonotonic magnetic field profile that is linearly related to the HTF electrostatic potential (e.g., $\delta\Phi^{HT} = 2.4\delta B$). Results indicate that much of the complex structure of the electron distribution function can be explained by the adiabatic motion of electrons in the smooth electromagnetic fields. Imprints associated with the ballistic transport of electrons from the different sources are easily identified and are organized by the separatrix boundaries computed using the shock macroscopic electric and magnetic fields. The Liouville predictions on the electron distribution function are in reasonable agreement, where a correspondence can be made, with the observed distribution functions throughout the shock layer, recovering much of the structural variations of the observed distribution function in response to the shock electromagnetic forces. Discrepancies between the V-L theory and the observations are difficult to ascertain and may be explained by (1) inaccuracies in computing the electron orbit, (2) 1-D assumption, (3) variations in the plasma properties and the magnetic field over the 3-s sampling time, and/or (4) wave-particle relaxation. The correspondence of the signatures of the electron distribution function with the variations in the macroscopic electric and magnetic fields provides the best evidence of parallel electric fields and their variation across collisionless shocks to date (direct observations of the parallel electric field have been hampered by the fact that the parallel electric field is relatively weak compared to the more dominant motional component). Also, no phase space holes are observed in the electron distribution function. Access to these "exclusion" regions of phase space cannot be explained by the 1-D steady state V-L approach as defined by the upstream and downstream spatial boundaries.

The complicated topology of the exclusion regions associated with nonmonotonic electric and magnetic fields may lead to spatially dependent free energy sources and hence spatial dependencies in the properties of the waves associated with irreversible filling of these non-

standard trapped electron regions of phase space. The detailed analysis of the electron distribution function and possible effects associated with the inherent 3-D character of the Earth's bow shock are left for future work.

References

Alfvén, H., and C. G. Fälthammer, *Cosmical Electrodynamics*, 2nd ed., Clarendon, Oxford, England, 1963.

Bale, S. D., P. J. Kellogg, D. E. Larson, R. P. Lin, K. Goetz, and R. P. Lepping, Bipolar electrostatic structures in the shock transition region: Evidence of electron phase space holes, *Geophys. Res. Lett.*, 25, 2929–2932, 1998.

Balikhin, M., and M. Gedalin, Kinematic mechanism of electron heating in shocks: Theory versus observations, *Geophys. Res. Lett.*, 21, 841–844, 1994.

Balikhin, M., M. Gedalin, and A. Petrukovich, New mechanism for electron heating in shocks, *Phys. Rev. Lett.*, 70, 1259–1262, 1993.

Coroniti, F. V., M. Ashour-Abdalla, and R. L. Richard, Electron velocity space hole modes, *J. Geophys. Res.*, 98, 11,349–11,358, 1993.

Feldman, W. C., Electron velocity distributions near collisionless shocks, in *Collisionless Shocks in the Heliosphere: Reviews of Current Research, Geophys. Monogr. Ser.*, vol. 35, edited by B. T. Tsurutani and R. G. Stone, pp. 195–205, AGU, Washington, D. C., 1985.

Feldman, W. C., J. R. Asbridge, S. J. Bame, M. D. Montgomery, and S. P. Gary, Solar wind electrons, *J. Geophys. Res.*, 80, 4181–4196, 1975.

Feldman, W. C., S. J. Bame, S. P. Gary, J. T. Gosling, D. J. McComas, and M. F. Thomsen, Electron heating within the Earth's bow shock, *Phys. Rev. Lett.*, 49, 199–201, 1982.

Feldman, W. C., S. J. Bame, S. P. Gary, J. T. Gosling, D. J. McComas, M. F. Thomsen, G. Paschmann, and M. M. Hoppe, Electron velocity distributions near the Earth's bow shock, *J. Geophys. Res.*, 88, 96–110, 1983.

Gedalin, M., Two-stream instability of electrons in the shock front, *Geophys. Res. Lett.*, 26, 1239–1242, 1999.

Gedalin, M., and E. Griv, Role of overshoots in the formation of the downstream distribution of adiabatic electrons, *J. Geophys. Res.*, 104, 14,821–14,825, 1999.

Goodrich, C. C., and J. D. Scudder, The adiabatic energy change of plasma electrons and the frame dependence of the cross-shock potential at collisionless magnetosonic shock waves, *J. Geophys. Res.*, 89, 6654–6662, 1984.

Gurnett, D. A., Plasma waves and instabilities, in *Collisionless Shocks in the Heliosphere: Reviews of Current Research, Geophys. Monogr. Ser.*, vol. 35, edited by B. T. Tsurutani and R. G. Stone, pp. 207–224, AGU, Washington, D. C., 1985.

Hull, A. J., Partition of temperature between electrons and ions across collisionless, fast mode shocks, Ph.D. thesis, Univ. of Iowa, Iowa City, 1998.

Hull, A. J., and J. D. Scudder, Model for the partition of

temperature between electrons and ions across collisionless, fast mode shocks, *J. Geophys. Res.*, *105*, 27,323–27,341, 2000.

Hull, A. J., J. D. Scudder, L. A. Frank, W. R. Paterson, R. J. Fitzenreiter, C. T. Russell, S. Kokubun, and T. Yamamoto, Coherent electron heating and phase space signatures at strong shocks (abstract), *Eos Trans. AGU*, *78*(17), Spring Meet. Suppl., S281, 1997.

Hull, A. J., J. D. Scudder, L. A. Frank, W. R. Paterson, and M. G. Kivelson, Electron heating and phase space signatures at strong and weak quasi-perpendicular shocks, *J. Geophys. Res.*, *103*, 2041–2054, 1998.

Hull, A. J., J. D. Scudder, R. J. Fitzenreiter, K. W. Ogilvie, J. A. Newbury, and C. T. Russell, Electron temperature and de Hoffmann-Teller potential change across the Earth's bow shock: New results from ISEE 1, *J. Geophys. Res.*, *105*, 20,957–20,971, 2000.

Knight, S., Parallel electric fields, *Planet. Space Sci.*, *21*, 741–750, 1973.

Lepping, R. P., et al., The Wind magnetic field investigation, *Space Sci. Rev.*, *71*, 207–229, 1995.

Lin, R. P., et al., A three-Dimensional plasma and energetic particle investigation for the wind spacecraft, *Space Sci. Rev.*, *71*, 125–153, 1995.

Matsumoto, H., H. Kojima, Y. Kasaba, T. Miyake, R. R. Anderson, and T. Mukai, Plasma waves in the upstream and the bow shock regions observed by GEOTAIL, *Adv. Space Res.*, *20*, 683–693, 1997.

Montgomery, M. D., J. R. Asbridge, and S. J. Bame, Vela 4 plasma observations near the Earth's bow shock, *J. Geophys. Res.*, *75*, 1217–1230, 1970.

Newbury, J. A., C. T. Russell, and M. Gedalin, The ramp widths of high-Mach-number, quasi-perpendicular collisionless shocks, *J. Geophys. Res.*, *103*, 29,581–29,593, 1998.

Schwartz, S. J., M. F. Thomsen, S. J. Bame, and J. T. Stansberry, Electron heating and the potential jump across fast mode shocks, *J. Geophys. Res.*, *93*, 12,923–12,931, 1988.

Scudder, J. D., The field-aligned flow approximation for electrons within layers possessing a normal mass flux: A corollary to the deHoffmann-Teller theorem, *J. Geophys. Res.*, *92*, 13,447–13,455, 1987.

Scudder, J. D., A review of the physics of electron heating at collisionless shocks, *Adv. Space Res.*, *15*(8/9), 181–223, 1995.

Scudder, J. D., A. Mangeney, C. Lacombe, C. C. Harvey, T. L. Aggson, R. Anderson, J. T. Gosling, G. Paschmann, and C. T. Russell, The resolved layer of a collisionless, high β, supercritical, quasi-perpendicular shock wave, 1, Rankine-Hugoniot geometry, currents, and stationarity, *J. Geophys. Res.*, *91*, 11,019–11,052, 1986a.

Scudder, J. D., A. Mangeney, C. Lacombe, C. C. Harvey, and T. L. Aggson, The resolved layer of a collisionless, high β, supercritical, quasi-perpendicular shock wave, 2, Dissipative fluid electrodynamics, *J. Geophys. Res.*, *91*, 11,053–11,073, 1986b.

Scudder, J. D., A. Mangeney, C. Lacombe, C. C. Harvey, C. Wu, and R. Anderson, The resolved layer of a collisionless, high β, supercritical, quasi-perpendicular shock wave, 3, Vlasov electrodynamics, *J. Geophys. Res.*, *91*, 11,074–11,097, 1986c.

Tidman, D. A., and N. A. Krall, *Shock Waves in Collisionless Plasmas*, Wiley-Interscience, New York, 1971.

Viñas, A. F., and J. D. Scudder, Fast and optimal solution to the Rankine-Hugoniot problem, *J. Geophys. Res.*, *91*, 39–58, 1986.

Whipple, E. C., The signature of parallel electric fields, *J. Geophys. Res.*, *82*, 1525–1531, 1977.

Winske, D., M. Tanaka, C. S. Wu, and K. B. Quest, Plasma heating at collisionless shocks due to the kinetic cross-field streaming instability, *J. Geophys. Res.*, *90*, 123–136, 1985.

Winske, D., J. Giacalone, M. F. Thomsen, and M. M. Mellott, A comparative study of plasma heating by ion acoustic and modified two-stream instabilities at subcritical quasi-perpendicular shocks, *J. Geophys. Res.*, *92*, 4411–4422, 1987.

A. J. Hull, D. E. Larson and R. P. Lin, Space Science Laboratory, University of California, Berkeley, Berkeley, CA 94720. (ahull@ssl.berkeley.edu; davin@ssl.berkeley.edu; boblin@ssl.berkeley.edu)

J. D. Scudder, Department of Physics and Astronomy, University of Iowa, Iowa City, IA 52242. (jds@space-theory.physics.uiowa.edu)